

The Atmospheric Signature of Io's Prometheus Plume and Anti-Jovian Hemisphere: Evidence for a Sublimation Atmosphere*

Kandis Lea Jessup, Lowell Observatory, 1400 W Mars Hill Rd, Flagstaff, AZ, 86001

John R. Spencer, Lowell Observatory, 1400 W Mars Hill Rd, Flagstaff, AZ, 86001

Gilda E. Ballester, Lunar and Planetary Laboratory, University of Arizona,
Tucson, AZ 85271

Robert R. Howell, Dept. Geology and Geophysics, University of Wyoming,
Laramie, WY 82071

Fred Roesler, Department of Physics, University of Wisconsin,
Madison, WI 53703

Miquela Vigel, Massachusetts Institute of Technology, Cambridge, MA 02139

Roger Yelle, Lunar and Planetary Laboratory, University of Arizona,
Tucson, AZ 85271

Submitted to *Icarus* April 30, 2002

Revised November 13, 2003

* Based on observations made with the NASA/ESA Hubble Space Telescope, obtained [from the Data Archive] at the Space Telescope Science Institute, which is operated by the Association of Universities for Research in Astronomy, Inc., under NASA contract NAS 5-26555. These observations are associated with program # 9119.

Figures: 11

Tables: 2

Io's Prometheus Plume and Anti-Jovian Atmosphere

Kandis Lea Jessup, Lowell Observatory, 1400 W Mars Hill Rd, Flagstaff, AZ 86001

Abstract

Using the Hubble Space Telescope's Space Telescope Imaging Spectrograph we have obtained for the first time spatially resolved 2000 – 3000 Å spectra of Io's Prometheus plume and adjoining regions on Io's anti-jovian hemisphere in the latitude range 60 N – 60 S, using a 0.1" slit centered on Prometheus and tilted roughly 45° to the spin axis. The SO₂ column density peaked at $1.25 \times 10^{17} \text{ cm}^{-2}$ near the equator, with an additional $5 \times 10^{16} \text{ cm}^{-2}$ enhancement over Prometheus corresponding to a model volcanic SO₂ output of 10^5 kg s^{-1} . Apart from the Prometheus peak, the SO₂ column density dropped fairly smoothly away from the subsolar point, even over regions that included potential volcanic sources. At latitudes less than $\pm 30^\circ$, the dropoff rate was consistent with control by vapor pressure equilibrium with surface frost with subsolar temperature $117.3 \pm 0.6 \text{ K}$, though SO₂ abundance was higher than predicted by vapor pressure control at mid-latitudes, especially in the northern hemisphere. We conclude that, at least at low latitudes on the anti-Jovian hemisphere where there are extensive deposits of optically-thick SO₂ frost, the atmosphere is probably primarily supported by sublimation of surface frost. Although the 45° tilt of our slit prevents us from separating the dependence of atmospheric density on solar zenith angle from its dependence on latitude, the pattern is consistent with a sublimation atmosphere regardless of which parameter is the dominant control. The observed drop in gas abundance towards higher latitudes is consistent with the interpretation of previous Lyman alpha images of Io as indicating an atmosphere concentrated at low latitudes. Comparison with previous disk-resolved UV spectroscopy, Lyman-alpha images, and mid-infrared spectroscopy suggests that Io's atmosphere is denser and more widespread on the anti-Jovian hemisphere than at other longitudes. SO₂ gas temperatures were in the range of 150-250 K over the majority of the anti-jovian hemisphere, consistent with previous observations. SO was not definitively detected in our spectra, with upper limits to the SO/SO₂ ratio in the range 1 – 10%, roughly consistent with previous observations. S₂ gas was not seen anywhere, with an upper limit of $7.5 \times 10^{14} \text{ cm}^{-2}$ for the Prometheus plume, confirming that this plume is significantly poorer in S₂ than the Pele plume ($S_2/SO_2 < 0.005$, compared to 0.08 – 0.3 at Pele). In addition to the gas absorption signatures, we have observed continuum emission in the near ultraviolet (near 2800 Å) for the first time. The brightness of the observed emission was directly correlated with the SO₂ abundance, strongly peaking in the equatorial region over Prometheus. Emission brightness was modestly anti-correlated with the jovian magnetic latitude, decreasing when Io intersected the torus centrifugal equator.

Keywords: Io, satellites, atmospheres, spectroscopy

Introduction

Io's atmosphere is one of the most unusual in the Solar System, and has proven to be an enigma complicated by the limitations of the attainable observations. The earliest Voyager, Pioneer and ground-based observations indicated that on-going volcanic activity, sublimation, and perhaps surface sputtering affect the composition, distribution and abundance of gases on Io (Fanale 1982). However, the relative importance of these processes has been difficult to determine. The SO₂ absorption signature first seen by Voyager IRIS, $2.6\text{-}20 \times 10^{17} \text{ cm}^{-2}$ or 5-40 nbar (Lellouch *et al* 1992) was consistent with either a volcanic plume at the volcano Loki or a global atmosphere in local vapor pressure equilibrium with surface frost at 119 – 126 K.

The first Earth-based constraints on the atmosphere came from disk-integrated observations in the UV, with the Hubble Space Telescope (HST) (Ballester *et al.* 1994, Trafton *et al.* 1996) and at millimeter (mm) wavelengths (Lellouch *et al.* 1992, Lellouch 1996). However, the derived SO₂ column densities have been model dependent, corresponding to $\sim 0.5\text{-}2 \times 10^{16} \text{ cm}^{-2}$ for a uniform hemispheric distribution of gas, to $\sim 0.6 - 3 \times 10^{17} \text{ cm}^{-2}$ for a localized distribution (11 – 36% of the disk), concentrated perhaps in the subsolar regions or near volcanic plumes.

Additional disk-integrated FOS observations in 1994 and 1996 of both the leading and trailing hemispheres were analyzed by Jessup *et al.* (2002). Best fits to these data indicated that Io's SO₂ atmosphere had both a $10^{15} - 10^{16} \text{ cm}^{-2}$ extended component at 110 – 350 K, and a $\sim 2.0 \times 10^{16}$ - 2.0×10^{17} confined component at 105-115 K. However, without spatial resolution across Io's disk the source of the high density component (volcanism or sublimation) could not be determined.

The first disk-resolved observations of the atmosphere were made with the HST Faint Object Spectrograph (FOS) by McGrath *et al.* (2000) in 1996, with good spatial (~ 750 km diameter circular FOV) and spectral resolution (4.4 Å FWHM effective resolution, after smoothing), and provided the first direct observations of the spatial variability of SO₂ and SO column densities, for the three distinct areas observed. SO₂ column densities were $\sim 1.5 \times 10^{16} \text{ cm}^{-2}$ at Ra (a bright low-latitude SO₂ frost region and possible active plume), $\sim 3.2 \times 10^{16} \text{ cm}^{-2}$ at Pele, (the site of a large but intermittent plume), and 0.7 cm^{-2} at a mid-latitude (45 S) region. Determination of control mechanisms was still ambiguous, however, due to limited spatial coverage and the intermittent nature of the volcanic plumes observed. While the enhancement at Pele was consistent with some volcanic control (if Pele was active), the drop in abundance at higher latitudes, if not due to the presence of plumes at Ra and Pele was consistent with hydrodynamic models of an atmosphere supported by frost sublimation (e.g., Wong and Johnson 1996).

The recent introduction of the Space Telescope Imaging Spectrograph (STIS) instrument on HST, which combines spectroscopy with imaging, has greatly advanced our ability to understand the Ionian atmosphere. STIS images of Io in reflected Lyman alpha light revealed bright high latitude/polar regions (above 60° N/S latitude) and dark equatorial regions (Roesler *et al.* 1999). Low-latitude attenuation of Lyman alpha light probably results primarily from absorption by SO₂ gas (Roessler *et al.* 1999, Feldman *et al.* 2000), though other species may also contribute. For example, the 300 K SO absorption cross-section at 1216 Å is 2.5 times larger than that of SO₂ (Nee and Lee 1986), so an SO gas column density $\sim 10^{15} \text{ cm}^{-2}$ (McGrath *et al.* 2000, Jessup *et al.* 2002), could significantly contribute to the attenuation of the Lyman alpha light. Determination

of absolute SO and SO₂ column densities is difficult due to uncertainties in the surface albedo variations and the interplanetary Lyman alpha background. In spite of these limitations, the FUV observations do provide important insights into the distribution of the absorbing constituents. A hemispherical distribution of optically thick SO or SO₂ gas is ruled out, and the atmosphere appears to extend all the way to the limb at low latitudes but is greatly reduced at mid to high latitudes, unless the low-latitude darkness near the limb is due to very low surface albedo rather than gas absorption. The low-latitude distribution of the atmosphere is consistent with atmospheric control by vapor pressure equilibrium with surface frost, though because the volcanic plumes are also equatorially concentrated, volcanic control is not ruled out (Strobel and Wolven 2001).

To better understand the spatial distribution of the atmosphere, we have obtained new STIS UV spectra of Io to map the distribution of the atmosphere across the disk with unprecedented spatial resolution and coverage. We include the volcanic plume Prometheus in our data to assess the role of volcanism in supplying the atmosphere, and to determine the composition of this prototype of the “Prometheus Class” plumes (McEwen and Soderblom 1983) in comparison to the larger, S₂-rich Pele plume that we observed previously (Spencer *et al.* 2000a). Because the Prometheus plume has been active in all observations from Voyager and Galileo (McEwen *et al.* 1998), we were confident that it would be active during our observations. From these data we document in detail the variation of SO and SO₂ column densities, and the SO₂ gas temperature, as a function of latitude and varying terrain type.

Observations and Data Reduction:

We obtained mid- to near- UV (2000-3170 Å) STIS reflectance spectra of the Prometheus plume and adjoining low- to mid-latitude regions on four separate days between November 4 and December 31, 2001 using the 0.1” slit, the NUV MAMA detector, and the G230L grating (see Table I). During the same observing period we also used two HST orbits to obtain 1140 – 1740 Å spectral images of Io using the G140L grating, the FUV MAMA, and the 2” slit to compare the Lyman alpha absorption images of Io’s atmosphere to its 2000 – 3170 Å spectroscopic signature. Implications of the G140L observations will be explored briefly in the discussion section, a more thorough presentation of the analysis of these data will be included in a later paper.

Centering the 0.1” slit over the Prometheus volcano (at 2° S, 153° W) and integrating for 900-1016 sec per exposure, we obtained 16 limb-to-limb long-slit mid- to near-UV spectra in 4 visits of two HST orbits each. In each case, Prometheus was near the center of Io’s disk and the slit was aligned at a 45° angle in the NW/SE direction (Io coordinates); constraints on the spacecraft roll angle prevented the use of a N/S or E/W orientation. The center of Io’s disk was located using the STIS onboard diffuse acquisition mode. We then performed the appropriate offset to Prometheus. Because these observations were obtained over a two-month period the data set may be more representative of the average atmospheric conditions than would be obtainable in a single “snapshot”. Although Io is fairly dim in the mid- and near-UV, the large volume of spectra also allows us to achieve adequate S/N.

These observations provide the most detailed look at Io at mid- to near-UV wavelengths obtained to date. The 0.1” slit is 2.5 times narrower than the aperture of the previous highest spatial

resolution observations (McGrath *et al.* 2000), and spatial resolution along the slit is even higher, about 0.05"/pixel. Our spectral range includes both the 2000-2200 Å region where the SO₂ and SO absorption cross-sections are largest, and also the 2500-3000 Å region where the S₂ absorption signature is strong. We also cover the SO₂ absorptions in the 2900 – 3100 Å region, which are ~ 10 times weaker than the SO₂ bands near 2100 Å and are sensitive to high column densities (>5 x10¹⁶ cm⁻²) of SO₂. The combination of the 1.55 Å/pixel dispersion of the G230L grating, 0.024"/pixel platescale of the NUV MAMA detector, and the 0.1" slit width provides a nominal spectral resolution of 6.5 Å full width half max (FWHM). While this resolution is lower than the 4-5 Å FWHM obtained when using the FOS and GHRS instruments (e.g., Ballester *et al.* 1994, Trafton *et al.* 1996), it is significantly higher than the 14 Å FWHM of the Galileo UVS instrument, and most importantly, it is sufficient to resolve the ~10 Å FWHM SO₂, SO and S₂ bands. Thus, these observations are the first to successfully simultaneously sample these spectral regions with spatial and spectral resolution adequate to define the variation in the gas signatures over an extended and latitudinally contiguous region of Io's surface. Finally, the use of the solar blind NUV MAMA detector strengthens the data quality in two ways. The first is that the data do not suffer from grating scattered light, unlike data obtained in the 1900-2100 Å region with the FOS instrument or the STIS CCD detector (McGrath *et al.* 2000, Baum *et al.* 1998, Spencer *et al.* 2000a). Secondly, there is no read noise in the NUV MAMA, giving 50% improvement in the signal-to-noise (S/N) near 2100 Å compared to the CCD detector.

Table I: Observations

	Image	Date (UT)	Start Time	Exp. Time (Sec)	Io Central Longitude	Io System-III Longitude	Io-sun dist. (AU)	solar phase (°)	grating
0	o6jna2a3q	11/04/01	21:49:11	960	140	167	5.15	9.9	G230L
1	o6jna2a4q	11/04/01	22:06:12	960	143	174	5.15	9.9	G230L
2	o6jnc2aaq	11/04/01	23:23:37	960	153	210	5.15	9.9	G230L
3	o6jnc2abq	11/04/01	23:40:38	1016	156	217	5.15	9.9	G230L
4	o6jna1s7q	11/22/01	14:39:07	960	143	95	5.15	7.7	G230L
5	o6jna1s8q	11/22/01	14:56:08	907	145	102	5.15	7.7	G230L
6	o6jnc1seq	11/22/01	16:27:35	960	158	146	5.15	7.7	G230L
7	o6jnc1sfq	11/22/01	16:44:36	907	161	152	5.15	7.7	G230L
8	o6jna3u1q	12/12/01	01:22:46	900	142	111	5.16	4.3	G230L
9	o6jna3u2q	12/12/01	01:38:47	900	144	119	5.16	4.3	G230L
10	o6jnc3u8q	12/12/01	02:57:43	900	156	151	5.16	4.3	G230L
11	o6jnc3u9q	12/12/01	03:13:44	900	158	169	5.16	4.3	G230L
12	o6jna4bwq	12/31/01	11:49:27	900	140	111	5.17	0.2	G230L
13	o6jna4bxq	12/31/01	12:05:28	900	142	119	5.17	0.2	G230L
14	o6jnc4c3q	12/31/01	13:25:04	907	153	157	5.17	0.2	G230L
15	o6jnc4c4q	12/31/01	13:41:12	900	156	164	5.17	0.2	G230L
L1	o6jn03bnq	12/13/01	18:59:25	900	135	194	5.16	4.0	G140L
L2	o6jn04tmq	12/29/01	18:03:08	900	145	40	5.04	0.6	G140L

We used the Space Telescope Science Data Analysis System (STDAS) CALSTIS reduction pipeline including flat-fielding, dark subtraction and absolute flux calibration. In order to maximize on-source integration time, we obtained wavelength calibration frames in a non-standard manner, during the Earth occultation period. This prevented use of the STIS pipeline wavelength calibration and geometric rectification routines, and we performed these tasks manually using the CALSTIS reduction programs **wavecal** and **x2d**. We also subtracted from

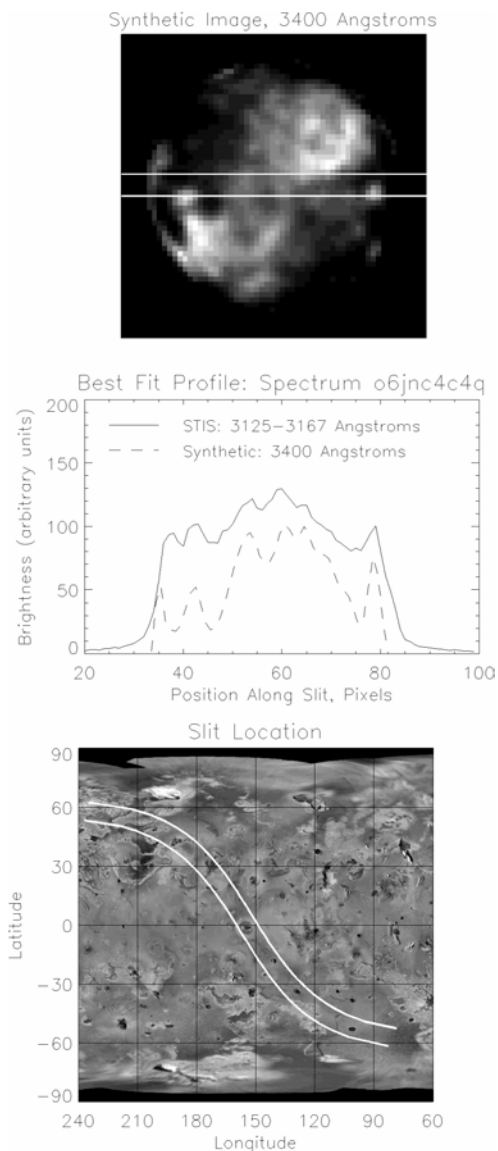


Figure 1: Illustration of the slit location procedure. First we create a synthetic 3400 Å image of Io (top) based on WFPC2 images, with the geometry of each STIS observation. North is to the upper left. For a synthetic slit of the appropriate width (white horizontal lines), we generate an along-slit brightness profile from this image and vary the slit position until a good visual match is obtained between features in the synthetic brightness profile and the actual 3125 – 3167 Å along-slit brightness profile seen in the STIS spectrum (middle). Note that differences in resolution and wavelength mean that the exact shape of the profile is not matched. The latitude and longitude of each point along the slit is then determined from the best-fit slit position (bottom).

the spectra wavelength-dependent background sky levels determined from locations in the slit distant from Io, correcting for negative sky values in the pipeline-reduced data.

We verified the accuracy of the slit location on Io by using the longest-wavelength portion of each spectrum (3120 – 3160 Å), which contains albedo features due to variations in SO₂ frost distribution, which correlate well with albedo patterns in the 3500 Å region, previously mapped by Voyager (McEwen 1988) and HST (Spencer *et al.* 1997). Because the central meridian longitude of Io at the time of each observation and the orientation of the STIS slit are well-constrained, and the location of Io’s limb in each spectrum is obvious, the only uncertainty was the slit location in the direction perpendicular to its length. To solve for this location, we constructed synthetic images of Io with the geometry of our actual observations, using global mosaics derived from HST Cycle 5 WFPC2 F336W 3500 Å images (Fig. 1). From these we determined intensity profiles expected for a 0.1” wide slit with the known STIS slit orientation, as a function of slit location on the disk. We determined the actual slit location for each STIS spectrum from the location of the along-slit profile derived from the WFPC2 images that best matched the 3120 – 3160 Å along-slit profile measured by STIS. In each case a good profile match was found, and we confirmed that the derived slit locations did indeed pass through the Prometheus volcano, and that the HST onboard targeting performed excellently. For each of our 16 rectified spectra we used the derived slit locations to determine the Io latitude and longitude of every 0.024” spatial pixel along the slit (Fig. 2).

Io’s 1.15 ± 0.05 ” diameter and the STIS spatial resolution of about 0.05” provided about 20 spatial resolution elements across Io along the slit of each long-slit spectrum. Additionally, unavoidable variations in central meridian longitude between observations lead to variation in the slit position at higher latitudes, giving greater longitudinal coverage there. Taking advantage of this, we re-

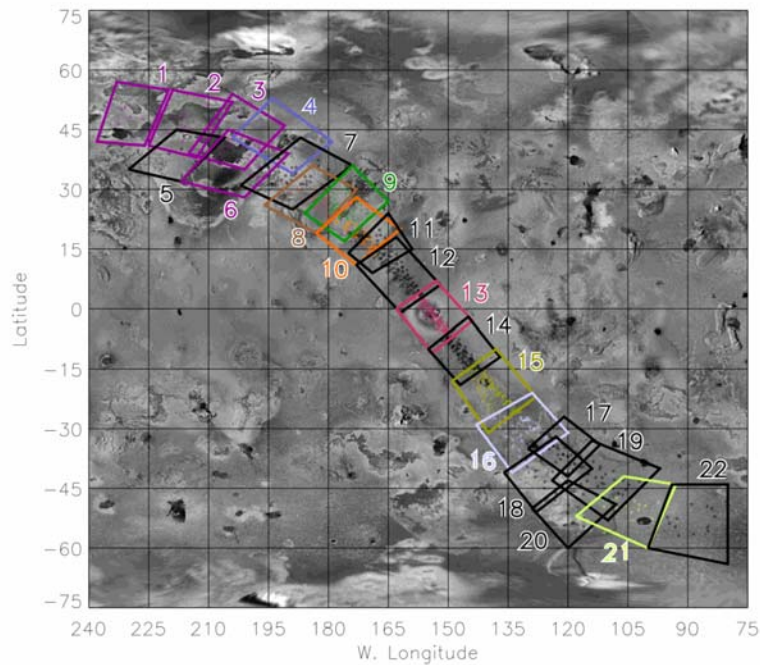


Figure 2: Spectrum bins. The location of the center of each pixel in our STIS data set is shown (black and colored dots) along with the area covered by the spectra in each of our spatial bins (see Table II). The colored bins correspond to locations of observed hotspots, plumes, or prominent calderas. The same color scheme is used throughout the paper to identify “volcanic” spatial bins.

binned each long-slit spectrum into 22 bins according to the slit-center latitude and longitude of each spatial pixel (Fig. 2, Table II). We then improved the signal-to-noise (S/N) in each bin by averaging each of the exposures together. Near the equator at Prometheus, the 0.1” slit width corresponded to approximately 320 km, or 10° of longitude; in this region we binned the spectra spatially into single ~10° latitude regions. At higher latitudes, where the longitudinal coverage was greater, multiple bins were created within a ~10° latitude bin, and this, along with projection effects, resulted in fewer

pixels being included in each bin. We also adjusted the chosen latitudinal extent of each bin as necessary to isolate specific surface features of interest, including Prometheus itself, other possible plume sites and hot spots, and prominent surface albedo features.

The observed spectra combine the signatures of the incident solar flux, atmospheric absorption and emission, and Io’s surface reflectance. To remove the solar spectral signature and estimate the albedo levels, we divided the rebinned Io spectra by a high resolution (0.5 Å sampling, 1.5 Å FWHM) solar spectrum acquire with the Solar Ultraviolet Spectral Irradiance Monitor (SUSIM) instrument flown on the second Atmospheric Laboratory for Applications and Science mission ATLAS-2, taken in April 1993 as provided by Van Hoosier (p.c. 1994) and published by Woods *et al.* 1996. We corrected for the known heliocentric distance, but made no correction for the solar phase angle, consequently the albedos we calculate are not absolute geometric albedos.

Prior to division, the solar spectrum was convolved and re-sampled to the effective STIS resolution. We found that the best cancellation of solar Fraunhofer lines was obtained using a Gaussian of 5.54 Å FWHM for the convolution, rather than the more complex line-spread profile (LSF) expected from convolution of the STIS point-spread function (Woodgate 1998) by the 0.1” slit. Subsequent 3-pixel smoothing then resulted in a 6.2 Å FWHM LSF, which we adopt as the effective spatial resolution of our data. Finally, small uniform corrections in the absolute

wavelengths of the rebinned Io spectra were determined by the alignment of the Fraunhofer absorption lines in the rebinned Io spectra with those in the solar spectrum.

Table II: Spectrum Binning and Model Fits

Bin	# pix. ^b	(latitude, longitude, Θ) ^c (°, °, °)	Significant Topographic Features	N(SO ₂) (cm ⁻²)	N(SO) (cm ⁻²)	T(SO ₂) (K)
1	6	(49, 231, -76)		1.3-2.8x10 ¹⁶	< 2.0x10 ¹⁵	115-325
2	14	(46, 214, -69)	N.W. Lei-Kung Fluctus	2.3-3.8x10 ¹⁶	< 2.0x10 ¹⁵	135-190
3	8	(45, 204, -61)	N.E. Lei-Kung Fluctus	4.8-8.8x10 ¹⁶	< 0.8x10 ¹⁵	275-575
4	11	(40, 194, -52)	Fo	2.3-3.8x10 ¹⁶	< 0.8x10 ¹⁵	105-165
5	4	(39, 217, -76)		0.6-1.3x10 ¹⁶	< 0.2x10 ¹⁵	105-135
6	23	(38, 202, -60)	S. Lei-Kung Fluctus	2.3-5.3x10 ¹⁶	< 2.0x10 ¹⁵	115-425
7	38	(33, 190, -50)	Bulicame Regio (bright)	2.8-6.8x10 ¹⁶	< 2.0x10 ¹⁵	165-425
8	34	(28, 183, -40)	unnamed caldera, Donar Fl.	1.8-6.8x10 ¹⁶	< 2.0x10 ¹⁵	105-525
9	32	(24, 177, -36)	Volund	1.8-6.8x10 ¹⁶	< 2.0x10 ¹⁵	135-625
10	53	(19, 171, -26)	Zamama	4.8-8.8x10 ¹⁶	< 4.0x10 ¹⁵	135-325
11	22	(15, 166, -21)		0.8-1.4x10 ¹⁷	< 8.0x10 ¹⁵	165-325
12	83	(8, 162, -15)	E. Colchis Regio (bright)	1.1-1.6x10 ¹⁷	< 6.0x10 ¹⁵	190-325
13	83	(-2, 154, 8)	Prometheus	1.4-2.4x10 ¹⁷	< 6.0x10 ¹⁵	190-375
14	67	(-11, 147, 13)		0.7-1.4x10 ¹⁷	< 6.0x10 ¹⁵	165-375
15	89	(-21, 138, 24)	Tupan	0.5-1.1x10 ¹⁷	< 2.0x10 ¹⁵	165-375
16	53	(-30, 130, 40)	Malik	1.8-8.8x10 ¹⁶	< 2.0x10 ¹⁵	135-775
17	20	(-35, 122, 45)		0.8-8.3x10 ¹⁶	< 2.0x10 ¹⁵	105-775
18	16	(-40, 123, 49)	N. Bactria Regio (bright)	1.8-7.3x10 ¹⁶	< 0.8x10 ¹⁵	225-775
19	38	(-42, 113, 56)		0.4-4.8x10 ¹⁶	< 2.0x10 ¹⁵	135-775
20	5	(-51, 119, 57)	S. Bactria Regio (bright)	0.6-3.8x10 ¹⁶	< 0.4x10 ¹⁵	425-775
21	15	(-50, 104, 65)	Catha Patera	0.04-1.8x10 ¹⁶	< 2.0x10 ¹⁵	105-775
22	13	(-53, 88, 74)		< 0.8x10 ¹⁶	< 2.0x10 ¹⁵	105-575

a : Results for albedos derived from the average of all magnetic longitudes per defined spatial bin. The results listed are the ± 1 sigma uncertainty range of the best fit.

b : the total number of individual spatial pixels (or spectra) averaged together per bin.

c : the average central latitude, longitude and solar zenith angle (Θ) of the points falling within each spatial bin. The average solar zenith angle is derived from the average central latitude within each bin and the average angular difference between the central longitude and the central meridian longitude (CML), using the simplifying assumption of zero solar phase angle. Although the CML varied between orbits, we found that within each bin the angular difference between the central longitude and the central meridian longitude per observation did not vary by more than 15°. The use of negatives in the listing of the solar zenith angle values is done solely for the purpose of identifying those observations taken pre-noon.

The data were clustered in Io's Jupiter System III longitude (Table I), with six observations near 110° W longitude, where Io passed through the centrifugal equator of the plasma torus (Dessler, 1983), and ten observations in the 146° – 217° longitude range, when the torus centrifugal equator was south of Io. Thus, we additionally binned the data into these two System III longitude groups to look for correlations between atmospheric behavior and Io's location relative to the torus.

Observational Trends:

Binned albedo spectra are presented in Figure 3. In most spectra the SO₂ gas absorption is evident in the strong SO₂ bands below 2300 Å and for a few cases in the weaker bands above 2800 Å. SO₂ gas absorption was strongest in the equatorial regions, and became weaker at higher latitudes, especially in the southern hemisphere. Discrete SO lines were not evident, but this is expected because they overlap the stronger SO₂ lines at the spectral resolution of our data. The strong S₂ lines in the 2600 – 2800 Å region, seen at Pele in 1999, were absent from all spectra. In the near-limb high-latitude spectra apparent albedos were lower, perhaps due in part to loss of light off Io’s limb due to the HST point-spread function (PSF). There was no obvious correlation between SO₂ absorption depths and Io’s position relative to the torus, but the magnitude of the “emission” features, prominent in low-latitude spectra near 2800 and 3000 Å, did seem to increase in the equatorial region when Io was south of the centrifugal equator. Because the “emission” features coincide with the deepest solar Fraunhofer bands, we believe they resulted from continuum emission, which by adding flux at all wavelengths above ~ 2400 Å reduced the apparent depth of the Fraunhofer lines on Io relative to the Sun.

Spectroscopic Albedo Model:

Variation in albedo A as a function of wavelength λ can be expressed as

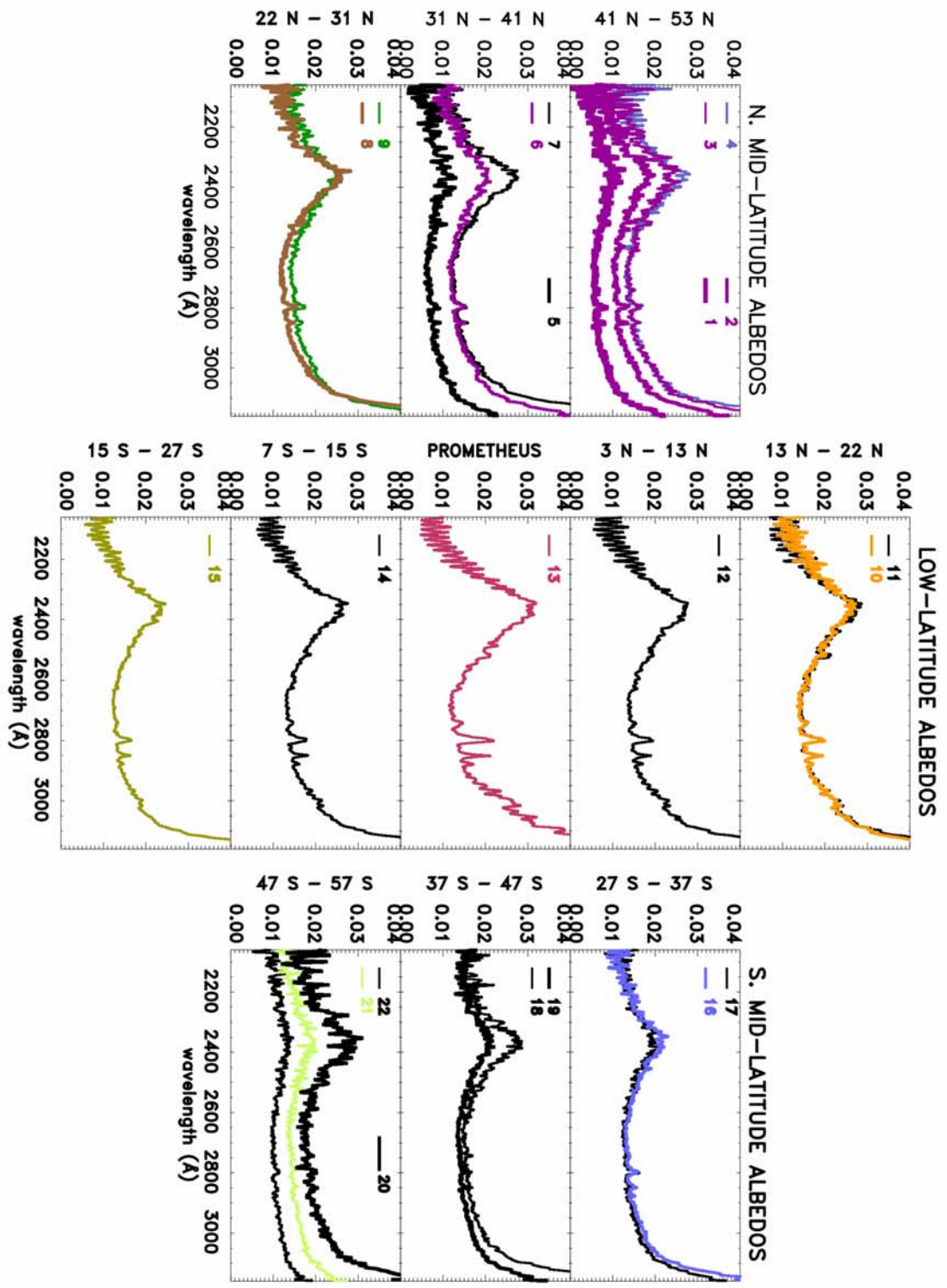
$$A(\lambda) = [R(\lambda) * S(\lambda, u(\theta, \varphi, N))]$$

Where, θ is co-latitude (90° - latitude), φ is longitude, $R(\lambda)$ is surface reflectance, and $S(\lambda, u(\theta, \varphi, N))$ is the atmospheric transmission, which is a function of the absorption path, u . u is defined as $2 * N / (\cos \delta\varphi \sin \theta)$, where N is the vertical atmospheric column density, and the factor of two results from the fact that the solar light passes through Io’s atmosphere twice; $\cos \delta\varphi \sin \theta$, is the cosine of the solar zenith angle; and, $\delta\varphi$ is the difference between φ and the central meridian longitude (CML). This formulation assumes that the sun and observer are in Io’s equator, and that solar phase angle is small, which are good approximations in the case for our observations (subsolar latitude = 2° , phase angle = $0.2 - 9.9^\circ$).

Surface Reflectance

We treat the surface reflectance term $R(\lambda)$ as a free parameter, defining its value at 50 Å wavelength increments and interpolating between these wavelengths by a cubic spline. This allows us to separate broad-scale spectral structure due to the surface reflectance from fine-scale structure due to gas absorption bands. Although the gas absorption also produces broad-scale structure due to overlap of absorption bands, fitting of the shape and depth of the band cores allows estimation of the broad-scale gas absorption independently of the surface reflectance (Fig. 4). The resulting surface reflectance compares favorably to the spectrum of SO₂ frost, though the match is not exact, indicating the probable presence of additional surface components.

Figure 3: Binned albedo spectra, identified by bin number. Continuum emission responsible for the apparent emission features near 2800 and 3000 Å (see text) has not been removed. In each case the absolute albedo levels are shown without offset.



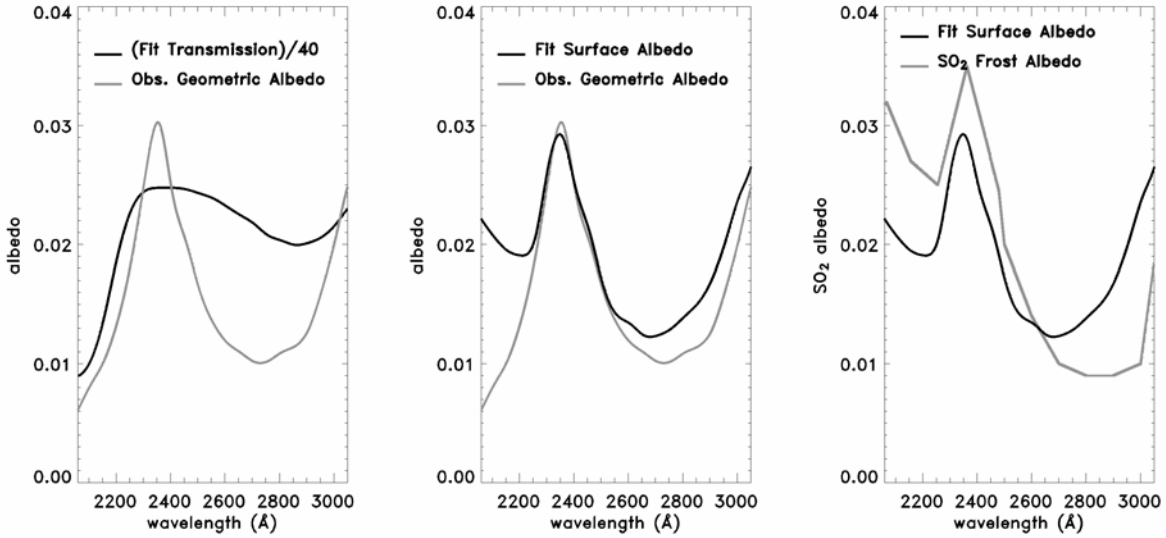


Figure 4: Low (50 Å sampling) spectral resolution comparison between the shape of the observed albedo spectrum in bin 13 (Prometheus), the fitted SO₂ and SO gas transmission, the fitted surface albedo $R(\lambda)$, and the laboratory spectrum of the SO₂ frost. At wavelengths greater than 2500 Å the SO₂ frost reflectance is that obtained by Nash *et al.* (1980) for medium grain size frost, shortward of 2500 Å the reflectance data are that provided by Hapke *et al.* (1981) but have been scaled to match the medium grain size measurements. The fitted surface albedo fits the SO₂ frost spectrum quite well.

Atmospheric Transmission

We assume that the atmospheric transmission is controlled by the molecules previously identified in the atmosphere: SO₂, SO, and S₂, and derive model absorption spectra for these molecules using techniques described in the Appendix. We first constrain just the SO₂ and SO abundances, using only the wavelength region extending from 2050-2300 Å that contains the strongest absorptions. Below 2050 Å the S/N is inadequate for fitting, and above 2300 Å the SO₂ and SO bands are weaker, and we do not have high resolution SO₂ absorption cross-section

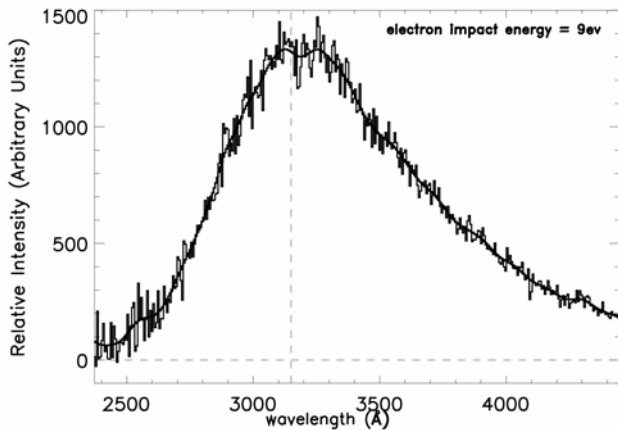


Figure 5: 9 eV SO₂ electron-impact fluorescence spectrum as measured by Ajello *et al.* (2002), showing both the raw spectrum and the heavily smoothed version used in our fits.

data as a function of temperature, or any SO absorption data above 2350 Å (see below). We use the short-wavelength SO₂ fit to predict the SO₂ absorption spectrum at longer wavelengths, and assume this spectrum when fitting the long-wavelength continuum reflectance and continuum emission levels (see below) for all spectra. We obtain an upper limit to S₂ abundance independently, because it does not have significant absorption in the 2050-2300 Å region, and there are no significant SO₂ and SO absorption bands in the region between 2600-

2700 Å where the S₂ absorption signature is strongest.

Continuum Emission Estimate

The continuum emission that is revealed by the mis-cancelled Fraunhofer lines in our albedo spectra is modeled on the assumption that it is due to electron impact induced emission from SO₂ gas, which is the probable source of diffuse 4040 Å emission seen in Galileo eclipse images (Geissler *et al.* 1999a, Geissler *et al.* 2001a). We assume the spectral distribution measured by Ajello *et al.* (2002) for an electron impact energy of 9 eV (Fig.5). We choose this electron energy because fluorescence spectra for higher electron energies show an SO emission feature at 2550 Å that is not evident in our data, and spectra for lower electron energies are not available. We also use the assumed emission shape to extrapolate the value of the 4040 Å flux detected in the Galileo SSI observations (Geissler *et al.* 1999a) to the 2800 Å region, in order to compare the

STIS observed emission with the SSI results. In the fitting of the continuum emission in the 2300 – 3200 Å region, we simultaneously include the SO₂ and SO absorption signature derived from the best-fit parameters in the 2050 – 2300 Å region.

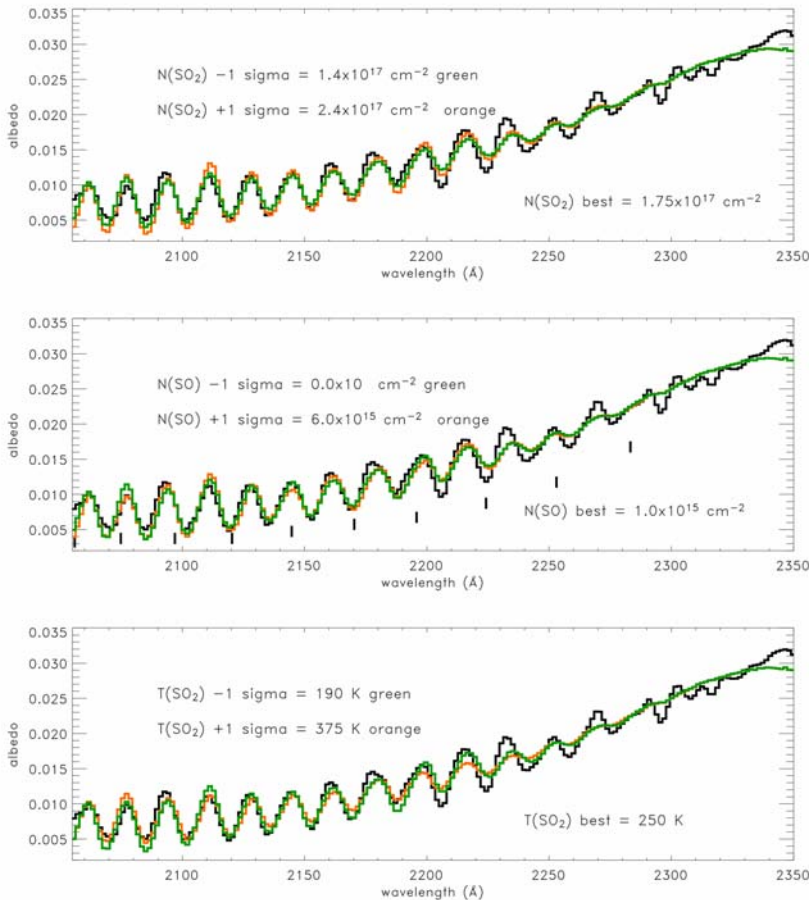


Figure 6: Illustration of the significance of the estimated uncertainties in our model fits for bin 13 (Prometheus). SO absorption band centers are marked in panel 2. In each panel, fits are shown with all parameters at their best-fit value except one, which is varied to $\pm 1\sigma$ from the best-fit value. The models underestimate SO₂ absorption above 2200 Å because we use low resolution SO₂ absorption cross-section data in this region. A full discussion of the cross-sections used in the model and how resolution affects the absorption behavior is provided in the Appendix.

Least Squares Fitting Procedure

Each of the parameters fit in our model are constrained from a grid search through a pre-defined parameter space. The SO₂ parameter space includes column densities in the range of 5.0×10^{14} - 6.5×10^{19} cm⁻²; and temperatures in the range 110 - 750 K. The SO parameter space includes column densities of 0.0 cm⁻², and in the range of 10^{14} - 5×10^{16} cm⁻². We varied the step sizes within the parameter space such that the SO₂ column density is fitted to within 10^{15} cm⁻²

from 10^{15} to 10^{16} cm^{-2} , to within 2.5×10^{15} from 10^{16} to 10^{17} cm^{-2} and within 1.25×10^{16} cm^{-2} from 10^{17} to 10^{18} ; the temperature is fitted to within 5 K from 105 to 115 K, within 10 K from 115 to 135 K, within 15 K from 135 to 190 K, and to within 25 K from 200 to 750 K; and the SO column density is fitted to within 10^{14} cm^{-2} from 10^{14} to 5.0×10^{14} cm^{-2} , to within 2.5×10^{14} cm^{-2} from 5.0×10^{14} to 10^{15} cm^{-2} , and to within 10^{15} cm^{-2} from 10^{15} to 5×10^{16} cm^{-2} . We fit continuum emission fluxes in the range of $0.011 - 11$ $\text{kRy } \text{\AA}^{-1}$ at 2800 \AA . The best-fit parameter values are derived from the least squares fit to the albedo weighted by the error in the albedos, which is estimated from the photon statistics of the Io spectra and the published uncertainties of the SUSIM solar spectrum. Spectrum S/N decreases with decreasing wavelength.

With the exception of those spectra in which a distinct SO_2 absorption signature was not evident, the minimum reduced chi-square value ranged from 0.8 to 1.8. Since these values are close to unity, indicating fits that are consistent with the data given the known uncertainties, the errors in the best-fit parameters are estimated by utilizing the 68 % confidence (or 1 sigma) intervals defined by the probability function of the χ^2 distribution, which is a function of the number of parameters used in the fit. Figure 6 illustrates our uncertainty estimation, by showing the fits to the Prometheus spectrum corresponding to the $\pm 1 - \sigma$ values of the SO_2 and SO number density, and SO_2 temperature. SO_2 number density controls band strength, SO number density dominates the spectrum shape at a few key wavelengths, such as the 2143 \AA region, and SO_2 temperature controls the central wavelength and skewness of the lines.

Results

Although we initially fitted the data after binning by latitude, longitude and magnetic longitude, only the continuum emission brightness showed significant dependence on magnetic longitude. Therefore, to improve S/N we re-binned the data by Io latitude and longitude only, ignoring magnetic longitude, and re-fitted the spectra. Spectral fits to the full dataset are presented in Figure 7 and the fitted parameter values are respectively, tabulated and presented graphically in Table II and Figure 8.

Figure 7: Fits (pink) to the binned albedo spectra (black), identified by bin number (see Figure 2 and Table II.) In (a) the westernmost longitudes are plotted so that the behavior as a function of latitude is shown, while in (b) fits to the data obtained at progressively eastward longitudes are shown for those latitudes with multiple longitude bins. In both (a) and (b) we show the fit to the albedos from $2050-2300 \text{ \AA}$ (left); and from $2650-3050 \text{ \AA}$ for the albedos derived with (middle) and without (right) the fitted continuum emission flux subtracted from the observed Io flux. Successive spectra are offset by 0.015, 0.01, and 0.012 in the left, middle, and right panels, respectively. We show the “fits” longward of 2970 \AA (green) to illustrate the presence of weak SO_2 bands in this wavelength range; however, here, where temperature dependence data are not available, the model albedo is calculated (not fitted) using the 300 K laboratory data (see the Appendix). Use of the high temperature SO_2 data at long wavelengths may partly explain the difficulties with removing all of the continuum emission above 2970 \AA at low latitudes (a, b), though these problems might also arise if the true wavelength dependence of the continuum emission differs from our assumed shape (Fig. 5).

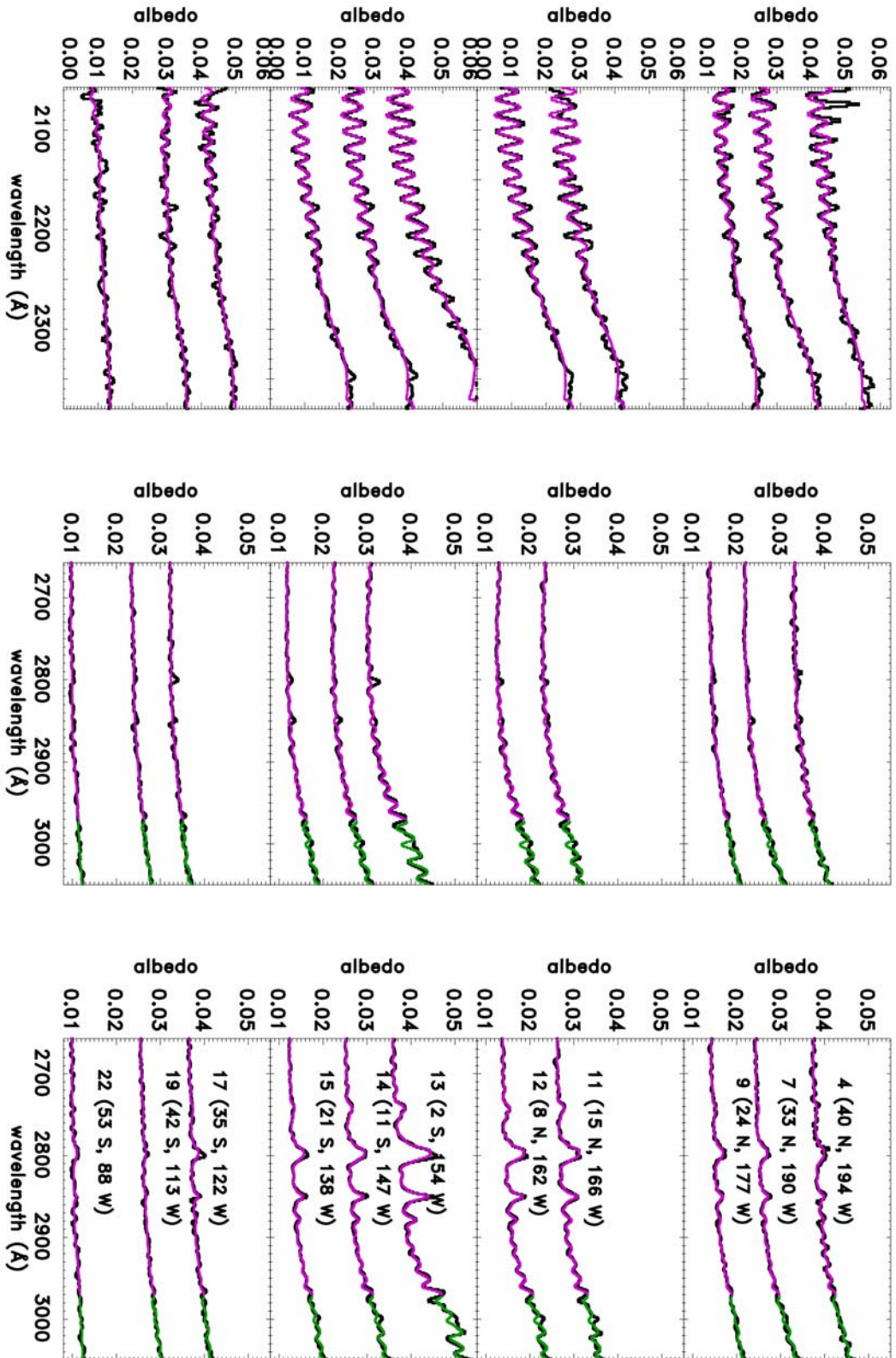


Figure 7a

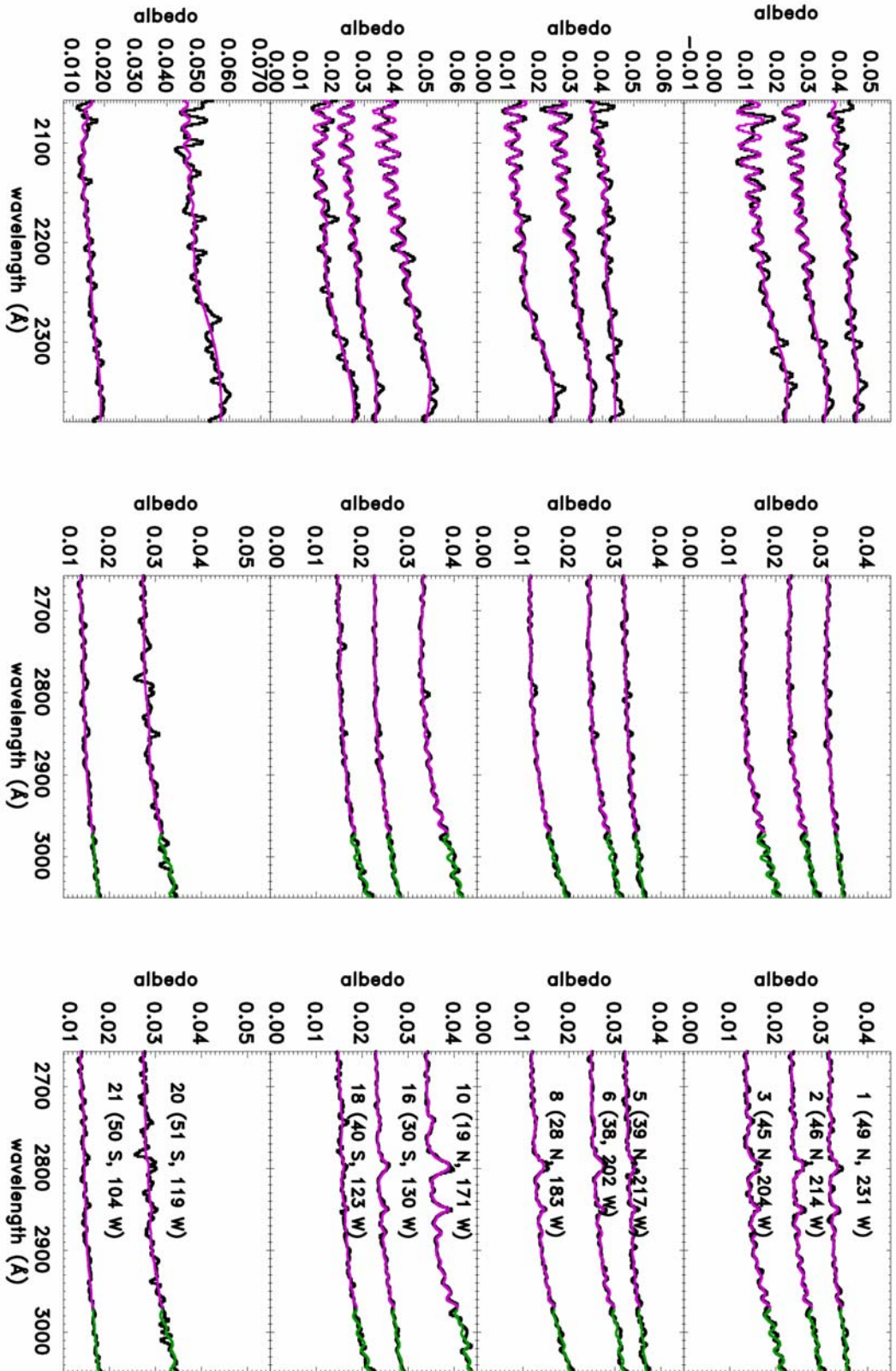


Figure 7b

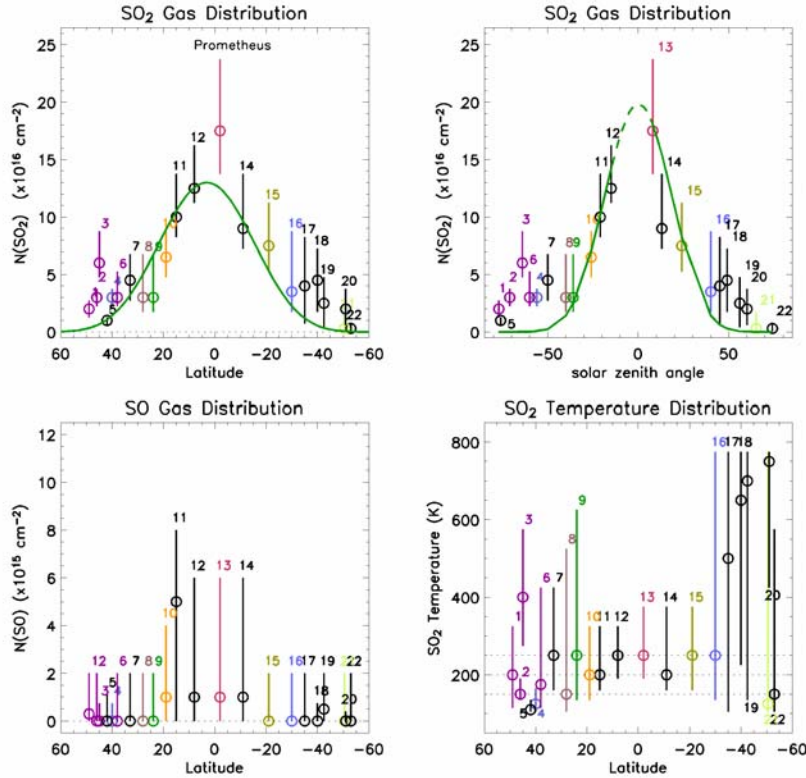


Figure 8: Best-fit atmospheric parameters as a function of location. Spatial bins are identified by color and number (Fig. 2, Table II). SO_2 number densities are compared to the values expected for vapor pressure equilibrium (Wagman 1979) with SO_2 frost temperatures in equilibrium with diurnally-averaged insolation, which is a function of latitude (top left) or instantaneous insolation, which is a function of solar zenith angle (top right). Corresponding peak frost temperature is 116.7 K (top left) and 118.0 K (top right). Negative solar zenith angle values are used to identify the northern hemisphere observations, which were obtained before local noon.

Volund (bin 9) plume sites, though it is possible that neither was active during our observations: the Zamama plume was intermittent and the Volund plume inactive during Galileo observations (McEwen *et al.* 1998), and Galileo observations of SO_2 frost grain size and abundance in this region did not show strong evidence for fresh SO_2 deposition (Douté *et al.* 2001). The active southern hemisphere hotspots Tupan, Malik and not recently active Catha (McEwen *et al.* 1998, Lopes-Gautier *et al.* 2001) also show no SO_2 enhancement, though in the northern hemisphere SO_2 column density over the hot spots Lei-Kung and Fo (McEwen *et al.* 1998, Spencer *et al.* 2000b, Lopes *et al.* 2001) is enhanced compared to the non-volcanic region in spatial bin 5.

Fitted SO_2 gas temperatures are mostly in the 150-250 K range, averaging ~ 200 K, broadly consistent with other UV observations (c.f. Ballester *et al.* 1994, McGrath *et al.* 2000). These temperatures are slightly higher than the 115-160 K expected for an atmosphere of column density $\sim 10^{16}$ - 10^{17} cm^{-2} solely influenced by solar radiation, perhaps due to some level of Joule heating in the atmosphere (Strobel *et al.* 1994). Fitted temperatures of ~ 110 -125 K are only found over Fo (bin 4) and a northern mid-latitude region (bin 5). Our ability to constrain useful

Because of the resolution of the data the SO_2 temperature constraints are broad. Additionally, variations in the SO_2 absorption strength appear to be controlled primarily by variations in column density. The fitted SO_2 column density is highest at low latitudes, peaking at $\sim 1.8 \times 10^{17}$ cm^{-2} over Prometheus, dropping to a few times 10^{16} cm^{-2} or less at mid-latitudes, with modestly higher densities at northern mid-latitudes than at the same latitudes in the south.

Except for the peak at Prometheus, there is little correlation of SO_2 column density with the presence of volcanic hotspots or plume sites (shown in color on Fig. 8). There is no SO_2 abundance peak at the Zamama (bin 10) or

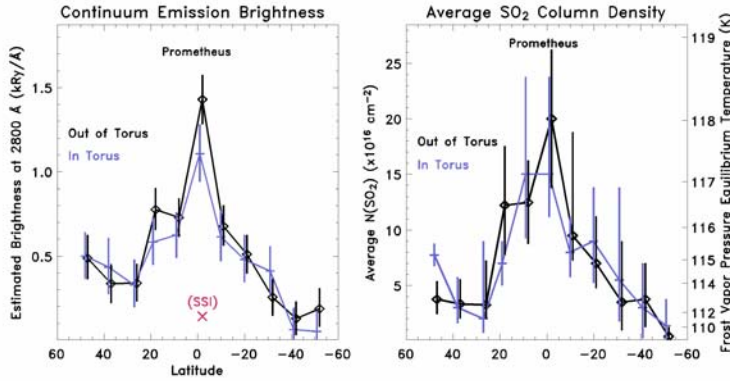


Figure 9: Comparison of the latitudinal variation of the fitted continuum emission brightness (left) with the fitted SO₂ column density (right), as a function of Io's position relative to the Io torus. The frost vapor pressure equilibrium temperature scale on the right is derived from derived the ideal gas law and the SO₂ vapor pressure curve (Wagman 1979)

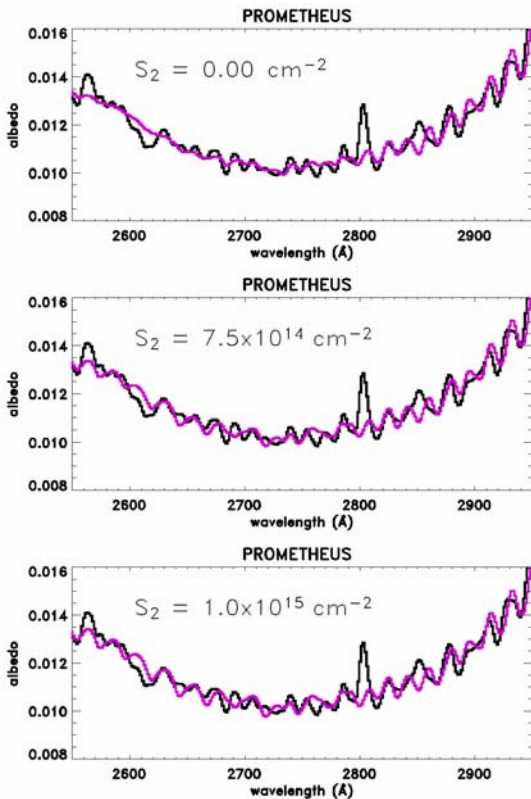


Figure 10: Derivation of S₂ upper limits. Our best-fit model (pink) for the observed Prometheus spectrum (black) is shown without S₂ (top), and with the addition of our chosen upper limit to the S₂ column density (middle), and with a higher column density (bottom) at which S₂ bands become more prominent than is consistent with our spectrum.

temperature information is inhibited by the resolution of the data, so that as the SO₂ band contrast decreases and/or the band shapes become more irregular the fitted SO₂ gas temperatures become less and less constrained, this is especially evident at mid-latitudes on the southern hemisphere.

We do not see a strong SO signature anywhere (with the possible exception of bin 11), and while the fit to many spectra is improved by addition of some SO, all 1-

sigma lower limits to SO abundance are consistent with zero. Because of the masking effect of the SO₂ bands, SO upper limits are higher in more SO₂-rich spectra. The upper limit to the SO/SO₂ ratio varies from 1 – 10%, roughly consistent with the 2 – 10% ratios obtained from disk-integrated mm wave data by Lellouch *et al.* (1996), and the 3 – 20 % ratios seen in the UV by McGrath *et al.* (2000).

Fitted continuum emission levels at 2800 Å are compared to SO₂ abundances, as a function of latitude, in Figure 9. Continuum emission brightness is modestly but significantly correlated with Io's position relative to the Io torus centrifugal equator, so that when Io is near the torus equator, the emission is generally lower than when the torus equator is south of Io. Emission varies by a factor of 5-10 with latitude for the regions observed, following the variations in SO₂ column density (and including the same N/S asymmetry at mid-latitudes), though the emission peaks more strongly over Prometheus than does the SO₂ column density.

The peak 2800 Å continuum emission brightness of 1.3 kilo-Rayleighs/Å is significantly higher than the 0.095 kRy/Å 4040 Å seen over Prometheus by Galileo SSI during eclipse (Geissler *et al.* 1999a), which would be equivalent to 0.14 kRy/Å at 2800 Å, assuming the 9 eV electron impact SO₂ emission spectrum from Figure 5. This discrepancy could be due to a difference in spectrum shape from the one we assume, time variability, and/or differences in viewing geometry.

Because S₂ is rapidly destroyed by photolysis, it is not expected in the atmosphere away from active plumes (Spencer *et al.* 2000a), but might plausibly be found in active plumes like Prometheus. We find that S₂ is not obvious in any of our spectra, independent of the absence or presence of a potentially active hotspot. Some subtle features in the Prometheus spectrum in the 2600 – 2800 Å region, such as the trough at 2665 Å and peak at 2678 Å, are matched better if a small amount of S₂ is added to the fit (Fig. 10), while the fit at 2770 Å is degraded. To be conservative, we claim no detection of S₂, and adopt an upper limit to the S₂ abundance of 7.5 x 10¹⁴ cm⁻² at Prometheus, giving an S₂/SO₂ ratio of < 0.005 at Prometheus.

Discussion:

Implications for the sublimation atmosphere

The most striking pattern in the data is the falloff in SO₂ abundance away from the subsolar point near the center of the disk, as would be expected from an atmosphere in vapor pressure equilibrium with surface frost heated by sunlight (Ingersoll *et al.* 1985, Moreno *et al.* 1991, Kerton *et al.* 1996). Because of the 45° tilt of our slit relative to Io's spin axis, we cannot tell whether abundance is more strongly correlated with solar zenith angle or latitude. Zenith angle control is expected if frost has low thermal inertia and its temperature is controlled by *instantaneous* equilibrium with sunlight. Latitude control is expected if frost temperature is controlled by equilibrium with *diurnally-averaged* sunlight, as might be the case if frost temperature varies little with local time, due to high thermal inertia or solid-state greenhouse effects (Veeder *et al.* 1994, Kerton *et al.* 1996), or if the atmosphere is supported by low-latitude plumes (Strobel and Wolven 2001). Latitudinal control is more consistent with the Lyman-alpha images unless the Lyman alpha albedo is strongly latitude-dependent (as is the case at longer wavelengths, c.f. Geissler *et al.* 1999b) and is much lower near the equator than near the poles, giving dark low latitudes regardless of SO₂ gas column abundance. In Figure 8 we explore these two cases, comparing the SO₂ column density variation to that expected from vapor pressure equilibrium with surface frost of constant albedo and either infinite thermal inertia (column density depends on latitude) or zero thermal inertia (column density depends on solar zenith angle). The latitude-dependent curve is not quite symmetrical about the equator because of the 2.0° N subsolar latitude at the time of the observations.

Subsolar/equatorial SO₂ column densities are consistent with vapor pressure equilibrium with SO₂ frost at a temperature of $\sim 117.3 \pm 0.6$ K. The decline in column abundance away from the subsolar point or equator is slightly faster in the zero thermal inertia model, but both models fit the data quite well for latitudes < $\sim 30^\circ$ or solar zenith angles < $\sim 40^\circ$, where dynamical sublimation models predict that column density will be controlled by vapor pressure (Moreno *et al.* 1991).

Further from the subsolar point or equator, the situation is more complicated. Southern hemisphere column abundances in bins 16 – 20 are barely consistent with equilibrium with infinite thermal inertia frost, and are too high for equilibrium with zero thermal inertia frost (assuming frost albedo and emissivity are uniform). Perhaps column densities here are enhanced by dynamical flow from higher-density regions (Ingersoll *et al.* 1985, Moreno *et al.* 1991), or by warm mid-latitude frost depleted surfaces that inhibit condensation (Ingersoll *et al.* 1989), though the latter explanation is unlikely as this area includes the bright frost region Bactria Regio. In the northern hemisphere the excess in observed column density compared to the vapor-pressure equilibrium curves is even more striking, perhaps due to an SO₂ source at the hot spots Lei-Kung and Fo, or simply inhibition of SO₂ condensation due to warm surface temperatures at the hot spots, as Lei-Kung in particular shows large areas of enhanced temperature (Rathbun *et al.* 2003).

Implications for the volcanic atmosphere

The only volcanic features where we detect obvious local enhancement of SO₂ column density are Prometheus, with its continuously-active plume, and perhaps Lei-Kung Fluctus and Fo Patera at northern mid-latitudes. The Prometheus data provides the first spatially resolved measurement of the composition and density of the prototype Prometheus-type plume, Prometheus itself.

Prometheus' S₂/SO₂ ratio of < 0.005 is at least 11-27 times lower than the ~ 0.08 – 0.3 S₂/SO₂ ratio observed at Pele (Spencer *et al.* 2000a). Thus, these observations provide the first direct evidence that the Prometheus plume is sulfur poor and significantly different in chemistry from the Pele plume, as originally proposed on the basis of plume heights and deposit colors by McEwen and Soderblom (1983). The chemical difference may result from the Prometheus plume's generation by sublimation of surface frosts by lava flows (Milazzo *et al.* 2001, Keiffer *et al.* 2000), compared to direct volcanic venting at Pele (Zolotov and Fegley, 2000). Several small diffuse red deposits, thought to result from condensation and breakdown of S₂ gas (Spencer *et al.* 2000a, Geissler *et al.* 1999b), are present within our slit (at Zamama, Tupan, Malik, and Prometheus itself), but S₂ gas is not seen above these deposits, either because the S₂ that creates them is below our detection threshold or the S₂ plumes were simply not active during our observations.

The Prometheus plume appears to be associated with a $5 \times 10^{16} \text{ cm}^{-2}$ local enhancement of SO₂ compared to background levels (Fig. 8). Applying the model of Ingersoll (1989) for estimating the pressure over a volcano of a given area, and assuming the radius of the Prometheus plume to be 150 km (Strom *et al.* 1981) the corresponding SO₂ output rate from Prometheus would be ~ 10⁵ kg/sec.

Ingersoll (1989) proposed that if a volcanic or sublimation source is neighbored by a cold frost (i.e. one on which condensation is occurring) then the atmospheric enhancement due to that source would fall off horizontally with length scale $L=(2\pi)^{1/2} (H/\alpha)$, where H is the scale height and α is the SO₂ sticking coefficient, which we assume to be 0.5. The SO₂ temperature derived from our data (i.e., 150 – 250 K) implies $L = 54 - 90 \text{ km}$. A source's influence can be extended if the surrounding surface is warm enough that its SO₂ vapor pressure exceeds the local plume pressure, preventing condensation, as might be the case in the near-subsolar regions neighboring

Prometheus. Equation A.29 of Ingersoll (1989), assuming $L = 54 - 90$ km, predicts even in this case, 10° (320 km) from the initial source the density would be 40% of its value near the source, which is significantly less than the 50 – 70% of the Prometheus density observed at 8° N and 12° S (Fig. 8, Table II). Thus, based on the Ingersoll model, the column density of SO_2 gas in the low latitude regions adjacent to Prometheus cannot be maintained by supply from the Prometheus plume, and must be maintained by another source, probably local frost sublimation as there are no major active volcanos in these regions. A falloff in column density away from Prometheus-type plumes within a ~ 100 km radius is confirmed by recent dynamical models (Zhang *et al.* 2003).

Comparisons with recent spatially resolved Galileo and HST UV observations

Spectroscopic observations of portions of the anti-jovian hemisphere of low spatial and spectral resolution over longitudes $120 - 150^\circ$ W were obtained by Hendrix *et al.* (1999) using the Galileo Ultraviolet Spectrometer (UVS). In this case, local SO_2 abundances as high as 1×10^{19} cm^{-2} , and global abundances near 4×10^{17} cm^{-2} , were inferred from the UVS data. In our new dataset, evidence of localized atmospheric patches is limited to the modest enhancement observed at Prometheus, and we can rule out local column densities approaching 10^{19} cm^{-2} over regions as large as our spatial resolution, because SO_2 abundances this high would produce much stronger absorption lines in the 3000 \AA region than we see in our data. It is possible that the Galileo UVS slit, which covered regions generally further east than our HST data, sampled a much denser part of Io's atmosphere. However, because the low UVS spectral resolution (14 \AA FWHM) could not resolve individual SO_2 absorption bands (10 \AA FWHM), and thus could not separate the spectral effects of gas and surface reflectivity, the large inferred gas abundances more likely result from erroneous assumptions about the surface reflectivity.

As previously discussed, the 1996 spatially resolved mid-UV HST/FOS observations of Pele (18° S, 257° W), Ra (7° S, 318° W), and "T3" (45° S, 300° W), all located on Io's trailing hemisphere (McGrath *et al.* 2000) found SO_2 abundances in the $\sim 0.7\text{-}3.2 \times 10^{16}$ cm^{-2} range. Similarly, sub-earth SO_2 column densities of $\sim 1\text{-}3 \times 10^{16}$ cm^{-2} were inferred from trailing hemisphere Lyman alpha observations obtained at longitudes of $243\text{-}272^\circ$ and $295\text{-}325^\circ$ W in 1997 and 1998, respectively (Feldman *et al.* 2000). While the 7.0×10^{15} cm^{-2} SO_2 column density observed by McGrath *et al.* over T3 (45° S latitude) is consistent with that derived in the current analysis from observations between 47° and 57° S latitude, they did not detect the high-density low-latitude atmospheric components inferred from mid-UV disk-integrated 1992 GHRS and 1996 FOS observations of the trailing hemisphere (Trafton *et al.* 1996, Jessup *et al.* 2002) or the spatially resolved 2001 STIS observations of the anti-jovian hemisphere presented here.

Although both sets of spatially resolved mid-UV observations were made near the subsolar point, McGrath *et al.* detected eight times less SO_2 over Ra (1.5×10^{16} cm^{-2}) than we detect in non-volcanic regions (bin 12) north of Prometheus (1.25×10^{17} cm^{-2}), despite the presence of bright frost and a possible plume at Ra. An even greater difference is implied in the non-volcanic atmospheres if the Ra observation included a contribution from the possible plume there. In fact, the SO_2 column densities observed over the probable volcanic plume sites Pele and Ra by McGrath *et al.* (2000) were both significantly lower than those seen in our new observations of volcanic or non-volcanic low latitude regions of the anti-jovian hemisphere.

There is no obvious simple explanation for this behavior. The mean bolometric albedo (Simonelli *et al.* 2001) is slightly lower in our bin 12 (north of Prometheus) than at Ra (0.45 vs. 0.50, respectively), but bin 14 just south of Prometheus (latitude 12 S) has the same albedo as Ra and much higher column density ($9 \times 10^{16} \text{ cm}^{-2}$). Likewise, recent analysis of SO₂ frost abundance obtained from the disk-resolved (200-500 km resolution) Galileo Near Infrared Mapping Spectrograph (NIMS) observations (Douté *et al.* 2001) indicates that the SO₂ frost abundances over Ra and our spatial bins 12 and 14 are comparable (40%, 48%, and 40% respectively), suggesting that SO₂ frost abundance cannot explain the difference either.

However, the hemispheric abundance of SO₂ frost, as inferred from near-UV spectroscopy and imaging (Nelson *et al.* 1980, McEwen *et al.* 1988) and near-IR spectroscopy (Howell *et al.* 1984), is greater on the anti-Jupiter hemisphere seen in our new data than the trailing hemisphere observed by McGrath *et al.* The Howell *et al.* analysis indicated that the SO₂ frost abundance on the hemisphere centered on 315° W was ~ 40 %, and ~85 % at 135° W. Perhaps this is part of the explanation for the differences in local SO₂ column abundances that we see between the hemispheres, but it is not clear why this global difference would affect the local gas abundance over regions with similar albedo and frost characteristics.

Further evidence for a denser and/or more extensive atmosphere on the anti-Jovian hemisphere than on the trailing hemisphere may come from the fact that recently-discovered 19 μm SO₂ gas absorption lines are strongest on the anti-Jovian hemisphere (Spencer *et al.* 2002), though interpretation of these data is still preliminary.

Significance of the SO₂ emissions

Galileo SSI recorded visible (4040 Å) emissions over volcanoes and the equatorial regions of Io (Geissler *et al.* 1999a, 2001a). These glows were inferred to be due to electron impact induced molecular SO₂ emission (Ajello *et al.* 1992, 2002), and appeared to be spatially correlated with active plumes. However, the localization over plumes was controversial because HST observations of far-UV atomic oxygen and sulfur emissions in the equatorial region showed that the FUV equatorial spots were at the location of the tangent points of Jovian magnetic field lines at the sub-Jovian and anti-Jovian points, and the brightness of these emissions increased when Io was closest to the centrifugal equator (Retherford *et al.* 2000). Later analysis of Galileo clear filter auroral images (Geissler *et al.* 2001a) found that the visible emissions were in fact present over the entirety of Io's disk, but were significantly enhanced over equatorial volcanic plumes, and in the equatorial region at the tangent points of the jovian magnetic field lines, with the plumes having the brightest emission levels. Geissler *et al.* (2001a) did not find any obvious correlations between the intensity of the equatorial or disk-averaged emissions and Io's System III longitude, but Cassini eclipse movies of Io's ~ 4000 Å continuum emission (Geissler *et al.* 2001b) clearly indicated that the location of emission at the magnetic tangent points was controlled by the changing orientation of Jupiter's magnetic field. Cassini also saw emission from volcanic plumes such as Tvashtar. Unfortunately, no study of the variation in the intensity of the volcanic and non-volcanic emission observed by Cassini at ~ 4000 Å as a function of magnetic longitude has yet been published.

Our new observations provide the first detection of continuum emission in the Ionian atmosphere near 2800 Å. The emission was directly correlated with the SO₂ abundance—peaking over the Prometheus region, and with the same N/S asymmetries (Fig. 9), consistent with an origin by electron impact induced SO₂ emission. The fact that emissions observed over Prometheus are enhanced relative to those observed over the lower SO₂ column density regions independent of the magnetic field orientation is consistent with the enhancement over plumes seen at visible wavelengths discussed above. We do not see an obvious change in the latitudinal distribution of the emission with magnetic longitude, as observed in other data sets, but this may be because the tangent-point emission, centered at longitude 180 W, is outside our slit which crosses the equator at longitude 155 W. The fact that the correlation of emission brightness with magnetic longitude is the opposite of that seen in the tangent point FUV atomic emission (Retherford *et al.* 2000) may also be due to the fact that the tangent point emission is outside our slit.

Insights to the electron energies that produced the observed NUV emission can also be derived from known emission behavior. Formation of SO through the dissociation of the SO₂ produces an emission peak at 2550 Å, but only occurs for impact energies greater than 10 eV. This emission peak is not seen in our data: attempts to remove the observed emission features with SO₂ fluorescence spectra obtained at energy levels of 11 eV and greater, result in the introduction of artificial absorption features near 2550 Å due to the over-subtraction of this peak. Consequently, we believe that the electron energy that excited the molecular SO₂ emission was below 10 eV. Electron energy was probably higher than 4 eV, the threshold energy for SO₂ excitation and dissociation. In addition, poor cancellation of Fraunhofer lines near 3000 Å, even after subtraction of the assumed SO₂ emission, in the low latitude region extending from 20° N to 32° S, may be evidence for an additional emission signature on top of the SO₂ emission near

3000 Å (Fig. 7). Possible sources for this are emissions induced from the electron impact of the SO and/or O molecules (J. Ajello pers. comm., 2002).

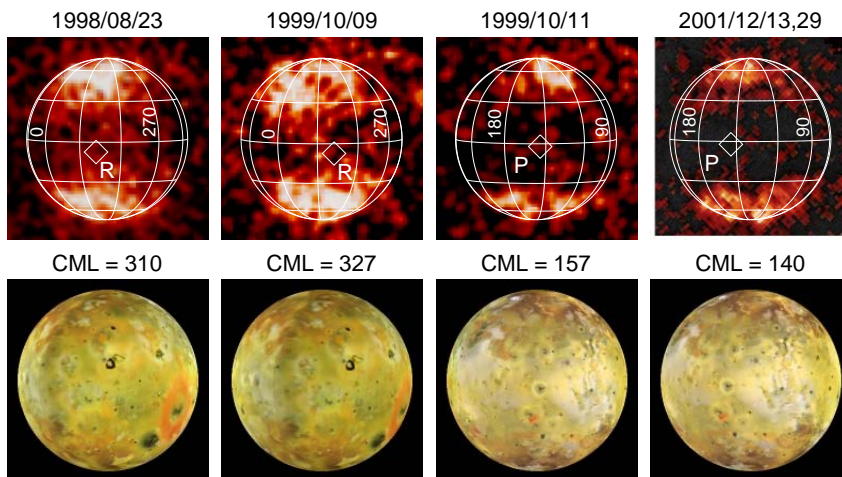


Figure 11: Longitudinal variability in Io's appearance in reflected Lyman alpha. We compare the average of our images of the hemisphere centered near Prometheus (see Table I), taken in December 2001 (top far right), to images of the same hemisphere (top center-right) taken two years prior, and to two images of the hemisphere centered near Ra taken in 1998 (top far-left, Feldman *et al.* 2000) and 1999 (top center-left, Ballester *et al.* 1999). The locations of Prometheus (P) and Ra (R) are indicated. The Lyman alpha attenuation on the Prometheus hemisphere extends to higher latitudes than on the Ra hemisphere. There was minimal temporal change in the appearance of the Prometheus hemisphere between 1999 and 2001.

Implications of the Lyman alpha observations

The new STIS Lyman alpha images of Io made nearly-simultaneously with our mid-UV spectra (Fig. 11) shows that as in previous Lyman-alpha images of Io (Feldman *et al.* 2000, Ballester *et al.* 1999), the poles are much brighter than low

latitudes, due either to latitude control of SO₂ gas abundance, low Lyman alpha albedo at low latitudes, or a combination, as discussed above. Comparison of our new images with previous Lyman alpha observations taken on August 23, 1998 (Feldman *et al.* 2000) and October 8 and 11, 1999 (Ballester *et al.* 1999) also indicates that the latitude of the boundary of the equatorial attenuation varies with longitude (Fig. 11). The latitude region of Lyman alpha attenuation ranges from $\sim \pm 30^\circ$ for images centered at 310° and 327° W, to $\sim \pm 45^\circ$ latitude, for images centered at 140° and 157° W, and there is an indication of increased attenuation at mid-latitudes towards the anti-Jovian (right) side in the trailing-hemisphere images. If, as the current observations indicate, the SO₂ gas abundance is the primary driver for the attenuation of the Lyman alpha light, then these Lyman alpha observations provide further evidence that latitudinal extent of the atmosphere, and by extension perhaps also its equatorial density, is consistently smaller at longitudes near Ra (318° W) than at longitudes near Prometheus (153° W).

Summary:

Using the Hubble's Space Telescope Imaging Spectrograph with the 0.1" slit in the mid- to near-ultraviolet (2000-3170 Å) we have obtained for the first time spatially and spectrally resolved UV spectra of Io's atmosphere extending continuously from the equatorial region to $\pm 50^\circ$ latitude. These observations provide insights into the influence of sublimation and volcanism on the overall Ionian atmosphere. We come to the following conclusions:

1) SO₂ column density peaks near the subsolar point, with large column densities (up to $1.8 \times 10^{17} \text{ cm}^{-2}$) and drops fairly smoothly towards the limb and higher latitudes even in regions without obvious volcanic sources. Because of the 45° tilt of the 0.1" slit, we cannot separate center-to-limb or time of day variations from latitudinal variations, but at low latitudes the pattern is consistent with a sublimation atmosphere regardless of which parameter is the dominant control. Therefore, at least at low latitudes on the anti-jovian hemisphere, where bright frost deposits are abundant, sublimation of surface SO₂ frost appears to be the main control of atmospheric pressure. While it is possible that an equatorial concentration of volcanic SO₂ sources could mimic the atmospheric distribution expected for sublimation control, we consider this a less likely explanation because (1) only at Prometheus do we see a strong peak associated with an active volcano, that peak is smaller than the background gas abundance, and the falloff away from this peak is slower than expected for a single volcanic source, and (2) the shape of the distribution is a good quantitative match to that expected for sublimation support of the atmosphere.

2) A modest but, significant SO₂ excess ($5 \times 10^{16} \text{ cm}^{-2}$) compared to expectations from frost sublimation was seen over the Prometheus plume, corresponding to an SO₂ output rate of about 10^5 kg/sec .

3) While we do not see a definitive SO signature in our spectra, we derive upper limits to the SO/SO₂ ratio in the range of 1-10%, roughly consistent with previous SO observations.

4) We do not detect S₂ at Prometheus or elsewhere on the anti-jovian hemisphere. The Prometheus S₂/SO₂ ratio of < 0.005 is much lower than the ratio at Pele (0.08 – 0.3, Spencer *et al.* 2000a), confirming the chemical difference between the two classes of plumes first proposed by McEwen and Soderblom (1983).

5) In spite of similarities in the overall SO₂ frost abundances and surface albedos, the SO₂ column density detected in 2001 STIS observations over the low-latitude regions flanking Prometheus is 8 times higher than over the low latitude Ra area seen in 1996 spatially resolved FOS observations. The difference may indicate generally lower SO₂ gas abundance on the trailing hemisphere than on the anti-Jovian hemisphere, perhaps correlated with the global distribution of SO₂ frost. The qualitative appearance of Lyman-alpha images, and new ground-based mid-infrared spectroscopy of Io's atmosphere, provides further evidence for this global atmospheric asymmetry.

6) The first near-UV (2800 Å) detection of continuum emission from Io, probably SO₂ electron impact fluorescence, indicates that the emission is significantly enhanced over the Prometheus plume relative to lower density SO₂ regions on Io's disk, consistent with Galileo and Cassini observations of Io's aurorae at visible wavelengths. The emission strength is correlated with local SO₂ column density, and modestly anti-correlated with Io's position relative to torus centrifugal equator. The lack of the emission peak at 2550 Å associated with the dissociation of the SO₂ (energy threshold of 10 eV) leads us to believe that the electron energy that excited the molecular SO₂ emission was below 10 eV.

7) The SO₂ gas temperature on the majority of the anti-jovian hemisphere was in the range of 150-250 K, consistent with expectations from plasma heating in the atmosphere.

Appendix: Details of the Gas Absorption Models

Our model of SO₂ gas absorption is based on recent laboratory data with improved spectral resolution than data used in previous models of Io's UV SO₂ gas signature. We use 300 K data from Stark *et al.* (1999), with 1-3 mÅ sampling and 5-16 mÅ resolution between 2000 and 2200 Å, and from Rufus *et al.* (2003), with 5-7 mÅ sampling and 4-32 mÅ resolution between 2200 and 3200 Å. While these measurements do not completely resolve the individual rotational lines (~3 mÅ separation near 2100 Å), they have served to dramatically improve our knowledge of the SO₂ gas absorption cross-section spectrum.

Given the resolution of the SO₂ cross-section data, calculation of the SO₂ transmission by a band model is preferred over a line-by-line (LBL) calculation to account for saturation effects with computational efficiency. Since the strongly overlapping nature of the rotational lines implies that the envelope of the line clusters rather than the individual line properties are the defining characteristic of the absorption cross-section (Freeman *et al.* 1984, Ballester *et al.* 1994), distinction between Voigt, Lorentz or Doppler line shapes is not important; and, we calculate the SO₂ transmission using the Malkmus band model equation for a Lorentzian line profile (Zhu 1994). We derive the average transmission S within each 1.55 Å wavelength interval $\Delta\lambda$ (equal to the wavelength sampling of our data) using

$$S(\lambda, \theta, \varphi, N) = \exp\left(\frac{-\pi y(\lambda)}{2} \left[\left(1 + \frac{4\langle\sigma(\lambda)\rangle u(\theta, \varphi, N)}{\pi y(\lambda)} \right)^{1/2} - 1 \right] \right),$$

where $\langle \sigma(\lambda) \rangle$ is the average high-resolution cross section within $\Delta\lambda$, and y is a wavelength dependent parameter which accounts for curve of growth effects due to line saturation, and is proportional to the mean Lorentzian line width and inversely proportional to the average line spacing (Zhu, 1994). Line saturation effects only become significant when the optical depth, $\sigma N / y$, is significantly greater than 1.

Derivation of y is most efficiently done by using the frequency distribution method (Zhu 1994, Ballester *et al.* 1994). In brief, this method reorders and ranks the high-resolution absorption cross-section σ_i according to its absorption coefficient k and then labels it with a normalized frequency variable g per rank. The distribution of the absorption band strength can be evaluated both analytically and numerically using Malkmus' equations which define $g(k)$ as

$$g(k) = \frac{1}{2} \left\{ \exp(\pi y(\lambda)) \operatorname{erfc} \left[\frac{\sqrt{\pi y(\lambda)}}{2} \left(\sqrt{\frac{1}{\kappa}} + \sqrt{\kappa} \right) \right] + \operatorname{erfc} \left[\frac{\sqrt{\pi y(\lambda)}}{2} \left(\sqrt{\frac{1}{\kappa}} - \sqrt{\kappa} \right) \right] \right\},$$

where erfc is the complementary error function and κ is the dimensionless k -coefficient $\kappa = \sigma_i / \langle \sigma(\lambda) \rangle$. Using these relationships, and the 300 K Stark *et al.* data, the non-temperature dependent y parameter is derived from the least-squares fit between the numeric and exact k -distributions of the absorption coefficient. Throughout the observed 2000-3200 Å wavelength range the value of y ranged from ~ 1 to significantly greater than 1. For the range of temperatures utilized in the model the average maximum absorption cross-section ranges from $\sim 5 \times 10^{-18}$ to 10^{-17} cm² thus, optical thickness effects only become important for column densities $> 10^{18}$ cm⁻².

The availability of high-resolution SO₂ cross-section data at multiple temperatures also allows us to model the signature of the SO₂ cross-section as a function of temperature. Assuming that the temperature dependence in the cross-section is a function of the Boltzman distribution of the rotational energy levels we can reliably calculate the temperature dependence using the usual functional form:

$$\sigma(\lambda) = s_0(\lambda) / T^{1.5} \exp(-B(\lambda)/T)$$

where T is the temperature, the 1.5 exponent accommodates for the non-linear nature of the SO₂ molecule; σ is the absorption cross-section as a function of wavelength, B and s_0 are wavelength dependent constants, and B is derived from the comparison of the SO₂ cross-section measurements taken at two temperatures. This equation accommodates for increases in contrast of the absorption bands at lower temperatures, and the broadening of the bands (which leads to an apparent shift in the peak of the bands) at higher temperatures; both of which result from variation in the energy level populations as a function of temperature.

We determine temperature dependence of SO₂ absorption cross-section between 2000 and 2970 Å using the lab data obtained at 300 K, described above, and multiple datasets of varying resolution at temperatures at least 100 K cooler. In the critical 2000-2200 Å wavelength region we use the Rufus *et al.* (2001) data taken at 159 K with 3 mÅ sampling and 5-7 mÅ FWHM resolution as the low temperature standard. Previous analyses of Io's UV SO₂ signature (Ballester *et al.* 1994, McGrath *et al.* 2000) used the older Freeman *et al.* (1984) data taken at 213 K with 4 mÅ sampling and 20 mÅ FWHM resolution. Differences in spectral resolution

can lead to significant differences in the predicted behavior of the SO₂ molecule. For example, Freeman *et al.* found that both the peak and trough values of the SO₂ cross-section were 10% higher if the cross-section was sampled at 1 mÅ before smoothing the data to 20 mÅ FWHM resolution. Similarly, the peak and trough values evident in the 200 K SO₂ cross-section derived from the 159 K Rufus *et al.* and 295 K Stark *et al.* measurements degraded to 1.5 Å resolution (similar to the resolution of the McGrath *et al.* data) are higher than that obtained by degrading the Freeman *et al.* data to the same sampling and resolution. Calculation of the SO₂ transmission ($N = 3 \times 10^{16} \text{ cm}^{-2}$) at 200 K using the degraded Freeman *et al.* cross-section data results in absorption band depths that are $10 \pm 5\%$ lower than that obtained using the 1.5 Å (FWHM) cross-section derived from the higher resolution data. Thus, previous models of the atmospheric abundance of SO₂ on Io that have relied on the lower resolution measurements probably overestimated the actual density of SO₂ gas on Io by a modest $10 \pm 5\%$.

Between 2200 and 2400 Å the low temperature laboratory data with the best spectral resolution are still those of Freeman *et al.* (1984). So, in this region we derive the temperature dependence of the SO₂ absorption from the comparison of the Freeman *et al.* to the Martinez and Joens (1992) data as has been done previously (Ballester *et al.* 1994, Spencer *et al.* 2000a). Above 2400 Å, there are no high-resolution low-temperature measurements of the SO₂ cross-section, so to determine temperature dependence we use the low (500 mÅ) resolution 200 K Wu *et al.* (2000) data, which extend to 2970 Å. Because these measurements are of a resolution significantly lower than that of the Rufus *et al.* data, those data are degraded to the appropriate resolution at these wavelength regions. There is no temperature dependence information for SO₂ gas above 2970 Å, so in this wavelength range we calculate the transmission using the average SO₂ cross-sections derived from the 300 K Smith *et al.* (2000) data.

For SO, the only absorption cross-section measurement currently available is that obtained by Philips (1981) for the B³Σ⁻-X³Σ⁻ band (1900-2350 Å) at 300 K and low (0.8 Å FWHM) resolution, insufficient to resolve the fine details of the spectrum. In the absence of better laboratory data, and provided that the SO gas column density does not exceed the level of saturation (about 10^{17} cm^{-2} for a gas temperature of 300 K), the SO transmission S can be calculated by Beer's law, $S(\lambda, \theta, \varphi, N) = \exp(-\sigma(\lambda)u(\theta, \varphi, N))$.

S₂ absorption cross-sections for the B³Σ⁻-X³Σ⁻ band transition (2400-3200 Å) have not been directly measured in the laboratory. As outlined in Spencer *et al.* (2000a), the absorption cross-section for the S₂ molecule is calculated at the resolution of the observations based on the published values for the energy level constants for the ground electronic state (Smith and Hopkins 1981), the B state (Huber and Herzberg 1979, Merchant and Andrews 1980), and the spin-spin and spin-orbit constants (Meyer and Crosley 1973). Honl-London factors are calculated for intermediate coupling between Hund's case a and b (Tatum and Watson 1981). Vibration transition probabilities are from S. R. Langhoff and H. Patridge (p.c.). We assume a pre-dissociation lifetime of 52 ps for transitions terminating on levels $v'=8, j' > 57, v'=9, j' > 34, v' > 9$.

For each of the molecules used in the transmission model, the resolution of our data is matched by convolving the model absorption cross-section spectra, which are calculated at the

same 1.55 Å sampling as our data, with a 5.54 Å FWHM Gaussian and then smoothing by three 1.55 Å pixels.

Acknowledgements

Support for HST program #9119 was provided by NASA through a grant from the Space Telescope Science Institute, which is operated by the Association of Universities for Research in Astronomy, Inc., under NASA contract NAS 5-26555. Additional support came from NASA Planetary Geology and Geophysics grant NAG5-10497. We thank Tony Roman of the Space Telescope Science Institution for his assistance in planning the observations.

References

- Ajello, J. M., James, G. K., Kanik I., 1992. The Complete UV Spectrum of SO₂ by electron impact, paper 2. The Middle Ultraviolet Spectrum. *J. Geophys. Res.* **97**, 10501-10512.
- Ajello, M. J., Hansen, D. L., Beegle, L. W., Terrell, C. A., Kanik, I., Jeames, G. K., Makarov, O.P., 2002. The Middle Ultraviolet and Visible Spectrum of SO₂ by electron impact. *J. Geophys. Res.* **107**:A7, SIA 2-1, CiteID 1099, DOI 10.1029/2001JA000122
- Ballester, G.E., McGrath, M. A., Strobel, D. F., Zhu, X., Feldman, P.D., Moos, H.W., 1994. Detection of the SO₂ Atmosphere on Io with the Hubble Space Telescope. *Icarus* **111**, 2-17.
- Ballester, G. E., Feldman, P. D., Roesler, F. L., Moos, H. W., Oliverson, R. J., Woodward, R. C., Scherb, F., Smyth, W. H., Ben Jaffel, L., Strobel, D. F., Wolven, B. C., Retherford, K. D., 1999. Lyman Alpha Observations of Io with STIS/HST, *B. A. A. S.*, **31**, #78.06.
- Baum, S., Bohlin, R., Christensen, J., Debes J., Downes R., Ferguson. J., Gonnella, A., Goudfrooij, P., Hayes, J., Hodge, P., Hulbert, S., Katsanis, R., Keyes, T., Lanning, H., McGrath, M., Sahu, K., Shaw, R., Smith, E., Walborn, N., Wilson, J., Bowers, C., 1998. Space Telescope Imaging Spectrograph Instrument Handbook. Eds. N. Walborn and S. Baum, Association for Research in Astronomy, Inc.
- Dessler, A, 1983. Physics of the Jovian magnetosphere. Cambridge Univ. Press, Cambridge, UK and New York, USA.
- Douté, S., Schmitt, B., Lopes-Gautier, R., Carlson, R., Soderblom, L., Shirley, J., and the Galileo NIMS Team 2001. Mapping SO₂ Frost on Io by the Modeling of NIMS Hyperspectral Images. *Icarus*, **149**, 107-132.
- Douté S., Lopes-Gautier, R., Kamp, L. W., Carlson, R., Schmitt, B. and the Galileo NIMS Team 2002. Dynamics and Evolution of SO₂ Gas Condensation around Prometheus-like Volcanic Plumes on Io as Seen by the Near Infrared Mapping Spectrometer. *Icarus*, **158**, 460-482.
- Fanale, F. P., Banerdt, W. B., Elson, L. S., Johnson, T. V., Zurek, R. W. 1982. Io's surface - Its phase composition and influence on Io's atmosphere and Jupiter's magnetosphere. In *Satellites of Jupiter*. p. 756-781, University of Arizona Press.
- Feldman, P. D., Strobel, D. F., Moos, H. W., Retherford, K. D., Wolven, B. C., McGrath, M. A., Roesler, F. L., Woodward, R. C., Oliverson, R. J., Ballester, G. E., 2000. Lyman- Alpha Imaging of the SO₂ Distribution on Io. *Geophys. Res. Lett.*, **27**, 1787-1789.

- Freeman D. E., Yoshino, K., Esmond, J. R., Parkinson, W. H., 1984. High Resolution absorption cross section measurements of SO₂ at 2132K in the wavelength region 172-240 nm. *Planet. Space Sci.* **32**, 1125-1134.
- Geissler, P. E., McEwen, A. S., Ip, W., Belton, M. J. S., Johnson, T.V., Smyth, W., Ingersoll, A. P., 1999a. Galileo imaging of atmospheric emissions from Io. *Science* **285**, 870-874.
- Geissler, P.E., McEwen, A. S., Ip, W., Keszthelyi, L., Lopes-Gautier, R., Granahan, J., Simonelli, D., 1999b. Global color variation on Io. *Icarus* **140**, 265-282.
- Geissler, P., Smyth, W. H., McEwen, A. S., Ip, W., Belton, M. J. S., Johnson, T. V., Ingersoll, A. P., Rages, K., Hubbard, W., Dessler, A. J., 2001a. Morphology and time variability of Io's visible aurora. *J. Geophys. Res.* **106**, 26137-26146.
- Geissler, P., McEwen, A., Porco, C., 2001b. Cassini imaging of visible aurorae on Io and Europa. *Bull. Am. Astron. Soc.* **33**, #09.02.
- Hapke, B., Wells, E., Wagner, J., Partlow, W., 1981. Far-UV, visible, and near-IR reflectance spectra of frosts of H₂O, CO₂, NH₃ and SO₂. *Icarus* **47**, 361-367.
- Hendrix, A. R., Barth, C. A., Hord, C. W., 1999. Io's patchy SO₂ atmosphere as measured by the Galileo ultraviolet spectrometer. *J. Geophys. Res.* **104**, 11,817-11,826.
- Howell, R., Cruikshank, D. P., Fanale, F. P., 1984. Sulfur dioxide on Io: Spatial distribution and physical state. *Icarus* **57**, 83-92.
- Huber, K. P. and G. Herzberg 1979. Constants of Organic Molecules. Van Nostrand Reinhold, New York.
- Ingersoll, A. P., Summers, M. E., Schlipf, S. G., 1985. Supersonic meteorology of Io - Sublimation-driven flow of SO₂. *Icarus* **64**, 375-390.
- Ingersoll, A. P. 1989. Io meteorology: How atmospheric pressure is controlled locally by volcanoes and surface frost. *Icarus* **81**, 298-313.
- Jessup, K. L., Ballester, G. E., Combi, M., Zhu, X., Strobel, D. F., Clarke, J. T., 2002. Io's Changing Atmosphere. In the *Magnetospheres of the Outer Planets Conference Abstract Book*, p. 116, <http://www.jhuapl.edu/mop/abstract.html>.
- Kerton, C. R., Fanale, F. P., Salvail, J. R., 1996. The state of SO₂ on Io's surface. *J. Geophys. Res.* **101** 7555-7564.
- Kieffer, S. W., Lopes-Gautier, R., McEwen, A. S., Smythe, W., Keszthelyi, L., Carlson, R., 2000. Prometheus: Io's Wandering Plume. *Science*, **288**, 1204-1208.
- Lellouch E., Belton, M. J. S., DePater, I., Paubert, G., Gulkis, S., Encrenaz, T., 1992. The structure, stability, and global distribution of Io's atmosphere. *Icarus* **98**: 271-95.
- Lellouch, E., Strobel, D. F., Belton, M. J. S., Summers, M. E., Paubert, G., Moreno, R., 1996. The Detection of Sulfur Monoxide in Io's atmosphere. *Astrophys. J.* **459**, L107-L110.
- Lellouch, E. (1996). Urey Prize lecture. Io's atmosphere: Not yet understood. *Icarus* **124**, 1-21.
- London, J., Rottman, G. J., Woods, T. N., Wu, F., 1993. Time variations of solar UV irradiance as measured by the SOLSTICE (UARS) instrument. *Geophys. Res. Lett.* **20**, 1315-1318.
- Lopes-Gautier, R., McEwen, A. S., Smythe, W. D., Geissler, P. E., Kamp, L. W., Davies, A. G., Spencer, J. R., Keszthelyi, L., Carlson, R. W., Leader, F. E., Mehlman, R., Soderblom, L. A., and the Galileo NIMS and SSI Teams 2000. Active volcanism on Io: Global distribution and variations in activity. *Icarus* **140**, 243-264.
- Martinez, R. D., and Joens, J. A., 1992. SO₂ absorption Cross-section measurements from 197 to 240 nm. *Geophys. Res. Lett.* **19**, 277-279.
- McEwen, A. S and Soderblom, L. A., 1983. Two classes of volcanic plumes on Io. *Icarus* **55**,191-217.

- McEwen, A. S., 1988. Global color and albedo variations on Io. *Icarus*, **73**, 385-426.
- McEwen, A. S., Keszthelyi, L., Geissler, P., Simonelli, D. P., Carr, M. H., Johnson, T. V., Klaasen, K. P., Breneman, H. H., Jones, T. J., Kaufman, J. M., Magee, K. P., Senske, D. A., Belton M. J. S., Schubert, G., 1998 Active volcanism on Io as seen by Galileo SSI. *Icarus* **135**, 181-219.
- McGrath, M. A., Belton, M. J. S., Spencer, J. R., Sartoretti, P., 2000. Spatially Resolved Spectroscopy of Io's Pele Plume and SO₂ Atmosphere. *Icarus* **146**, 476-493.
- Merchant, V. E. and Andrews, M. L., 1980. Technique for measuring rotational temperature of microwave excited diatomic sulfur. *Appl. Opt.* **19** 3113-3117.
- Meyer, K. E. and Crosley, D. R., 1973. Rotational satellite intensities and triplet splitting in B-3Σ-U-State of S₂. *Can. J. Phys.* **51** 2119-2124.
- Milazzo, M. P., Keszthelyi, L. P., McEwen, A. S., 2001. Observations and initial modeling of lava-SO₂ interactions at Prometheus, Io. *J. Geophys. Res.*, **106**, 33121-33128.
- Moreno, M. A., Schubert, G., Kivelson, M. G., Paige, D., Baumgardner, J., 1991. Io's volcanic and sublimation atmospheres. *Icarus* **93**, 63-81.
- Nash, D. B., Fanale, F. P., Nelson, R. M., 1980. SO₂ frost - UV-visible reflectivity and Io surface coverage. *Geophys. Res. Lett.* **7**, 665-668.
- Nee, J. B. and Lee, L. C., 1986. Vacuum ultraviolet photoabsorption study of SO, *J. Chem. Phys.* **84**, 5303-5307.
- Nelson, R. M., Lane, A. L., Matson, D. L., Fanale, F. P., Nash, D. B., Johnson, T. V., 1980. Io longitudinal distribution of sulfur dioxide frost. *Science* **210**, 784-786.
- Phillips, L. F. 1981. Absolute Absorption Cross Section for SO between 190 and 235 nm. *J. Phys. Chem.*, **85**, 3994-4000.
- Rathbun, J., Spencer, J. R., Tamppari, L. K., Martin, T. Z., Barnard, L., Travis, L. D., 2003. Mapping of Io's thermal radiation by the Galileo Photopolarimeter-Radiometer (PPR) Instrument. *Icarus*, this issue.
- Retherford, K., Moos, H. W., Strobel, D. F., Wolven, B. C., Roesler, F. L., 2000. Io's equatorial spots: Morphology of neutral UV emissions. *J. Geophys. Res.* **105**:A12, 27157-27165.
- Roesler, F. L., Moos, H. W., Oliverson, R. J., Woodward Jr., R. C., Retherford, K. D., Scherb, F., McGrath, M. A., Smyth, W. H., Feldman, P. D., Strobel, D. F., 1999. Far-Ultraviolet Imaging Spectroscopy of Io's atmosphere with HST/STIS. *Science*, **283**, 353-357.
- Rufus, J., Stark, G., Smith, P. L., 2001. Low temperature SO₂ cross-sections, <http://cfa-www.harvard.edu/amdata/ampdata/so2159k.shtml>.
- Rufus, J., Stark, G., Smith, P., Pickering, J. C., Thorne, A. P., 2003. High-resolution photoabsorption cross section measurements of SO₂, 2: 220 to 325 nm at 295 K. *J. Geophys. Res.* **108**, E2, pp. 5-1, CiteID 5011, DOI 10.1029/2002JE001931.
- Simonelli, D. P., Dodd, C., Vevereka, J., 2001. Regolith variations on Io: Implication for bolometric albedoes, *J. Geophys. Res.*, **106**, 33241-33252.
- Smith, A. L. and Hopkins, J. B., 1981. Fluorescence of S₂(B-X) excited by fixed frequency ultraviolet lasers. *J. Chem. Phys.* **75**, 2080-2084.
- Smith, P. L., Rufus, J., Stark, G., Thorne, A. P., Pickering, J. C., 2001. High resolution photoabsorption cross section measurements of SO₂ at 295 K between 220 and 328 nm. American Astronomical Society, DPS meeting #33, #56.07
- Spencer, J. R., McEwen, A. S., McGrath, M. A., Sartoretti, P., Nash, D., Knoll, K., Gilmore, D., 1997. Volcanic resurfacing of Io: Post-HST repair imaging. *Icarus*. **127**, 221-237.

- Spencer, J. R., Jessup, K. L., Yelle, R., Ballester, G. E., McGrath, M. A., 2000 (a). Discovery of Gaseous S₂ in Io's Pele Plume. *Science* **24**, 1208-1210.
- Spencer, J.R., Rathbun, J. A., Travis, L. D., Tamppari, L. K., Barnard, L., Martin, T. Z., Martin, A. S., 2000 (b). Io's Thermal Emission from the Galileo Photopolarimeter-Radiometer. *Science* **24**, 1198-1201.
- Spencer, J. R., Jessup, K.L., Lellouch, E., Richter, M., Greathouse, T., Lopez-Valverde, M., Flaud, J.-M., 2002. Ground-Based Infrared Detection of Io's SO₂ Atmosphere. *B. A. A. S.*, **34**, 912.
- Stark, G., Smith, P. L., Rufus, J., Thorne, A. P., Pickering, J. C., Cox, G., 1999. High resolution photoabsorption cross-section measurements of SO₂ at 295K between 198 and 220 nm. *J. Geophys. Res.* **104**, 16585-16590.
- Strom, R. G., Schneider, N. M., Terrile, R. J., Cook, A. F., Hansen, C., 1981. Volcanic eruption on Io, *J. Geophys. Res.*, **86**, 8593-8620.
- Strobel, D. F., Zhu, X., and Summers, M. E., 1994. On the vertical thermal structure of Io's atmosphere. *Icarus* **10**, 18-30.
- Strobel, D. F., and Wolven, B. C., 2001. The Atmosphere of Io: Abundances and Sources of Sulfur Dioxide and Atomic Hydrogen. *Astrophysics and Space Science*, **277**, 271-287.
- Tatum, J. B. and Watson, J. K. G., 1971. Rotational Line strengths in Σ -3- Σ -3 transitions with intermediate coupling. *Can. J. Phys.* **49**, 2693.
- Trafton, L., Caldwell, J., Barnet, C., Cunningham, C. C., 1996. The gaseous sulfur dioxide abundance over Io's leading and trailing hemispheres: HST spectra of Io's C¹B₂--X¹A₁ band of SO₂ near 2100 Å. *Astrophys. J.*, **456**, 384, 6-C5.
- Veeder, G. J., Matson, D., Johnson, T., Blaney, D., Gougen, J., 1994. Io's heat flow from infrared radiometry: 1983-1993. *J. Geophys. Res.* **99**: E8, p. 17095-17162.
- Wagman, D. D. 1979. *Sublimation Pressure and Enthalpy of SO₂*. Chem. Thermodynamics Data Center. Nat. Bur. of Standards, Washington, D. C.
- Woodgate, 1998 (1997, HST Calibration Workshop with a new generation of instruments/ ed. Casertano, S. Jdrzejewski, R. Keyes, C. D. and M. Stevens, Baltimore, MD p. 60)
- Woods, T. N., Prinz, K. K., Rottman, G. J., London, J., Crane, P. C., Cebula, K. P., Hilsenrath, E., Brueckner, G. E., Andrews, M. D., White, O. R., VanHoosier, M. E., Floyd, L. E., Herring, L. C., Knapp, B. G., Pankratz, C. K., Reiser, P. A., 1996. Validation of the UARS solar ultraviolet irradiances: Comparison with the ATLAS 1 and 2 experiments. *J. Geophys. Res.* **101**, 9541-9569.
- Wong, M.C. and Johnson, R. E., 1996. A three-dimensional azimuthally symmetric model atmosphere for Io 1. Photochemistry and the accumulation of a nightside atmosphere. *J. Geophys. Res.* **101**, 23243-23254.
- Wu, R. Y. C., Yang, B. W., Chen, F. Z., Judge, D. L., Caldwell, J., Trafton, L. M., 2000. Measurement of high-, room-, and low-temperature photoabsorption cross sections of SO₂ in the 2080-2950 Å region, with application to Io. *Icarus* **145**, 289-296.
- Zolotov, M. and Fegley, Jr., B. 2000. Eruption conditions of Pele volcano on Io inferred from chemistry of its volcanic plume. *Icarus* **27**, 2789-2792.
- Zhang, J., Goldstein, D. B., Varghese, P. L., Gimelshein, N. E., Gimelshein, S. F., Levin, D. A., 2003. Simulation of gas dynamics and radiation in volcanic plumes on Io. *Icarus* **163**, 182-197.
- Zhu, X. 1994. An Accurate and efficient radiation algorithm for middle atmosphere models. *J. Atmos. Sci.* **51**, 3593—3614.